Available online at www.ijournalse.org

Emerging Science Journal

(ISSN: 2610-9182)

Vol. 10, No. 3, June, 2026

Hybrid Parametric and Non-Parametric Identification of PEMFC Dynamics in SISO and MIMO Workflow

Eduardo Benavides-Farías [1*], Abel Rubio-Roldán [1, 2], Wilton Agila [1, 2], Edwin Valarezo-Añazco [1]

[1] *Faculty of Electrical and Computer Engineering, Escuela Superior Politécnica del Litoral (ESPOL), Campus Gustavo Galindo Km 30.5 Vía Perimetral Guayaquil, Ecuador.*

[2] *Faculty of Electrical and Computer Engineering, CASE, CIDIS, Escuela Superior Politécnica del Litoral (ESPOL), Campus Gustavo Galindo Km 30.5 Vía Perimetral Guayaquil, Ecuador.*

Abstract

Reliable control-oriented models of PEM fuel cells remain challenging because PEMFC dynamics are nonlinear, coupled, and hard to excite under practical constraints. This paper presents a hybrid identification workflow in a controlled MATLAB/Simulink simulation environment. After discretization, bounded multisine excitation is applied, and correlation-based response analysis (CRA) is used to obtain non-parametric dynamics; low-order parametric structures (ARX, ARMAX, Box–Jenkins, OE, and FIR) and a grey-box state-space model are then estimated and validated using Fit%, information criteria (AIC/BIC), and residual diagnostics. In SISO, ARMAX provides the best accuracy–parsimony compromise (Fit = 96.84% with the lowest AIC/BIC and residuals mostly within confidence bounds), while Box–Jenkins achieves the highest fit (*i.e.*, 98.75%) at higher complexity. In MIMO, most channels achieve an accuracy over 92% fit, with the most coupled pathway remaining the limiting case (best fit = 86.38% with BJ), and ARMAX/BJ emerging as the dominant structures across channels. The grey-box model attains 97.35% fit for voltage and 86.47% for power. This paper establishes a unified, control-oriented hybrid workflow that links CRA non-parametric estimation with low-order parametric and grey-box models, providing compact, physically interpretable PEMFC dynamics and practical model-selection guidance for control and energy-management applications.

Keywords:

Correlation-Based Response Analysis;
Dynamic Modeling;
Grey-Box Modeling;
MIMO Systems;
Parametric Identification;
PEMFC; System Identification.

Article History:

Received:	03	January	2026
Revised:	19	May	2026
Accepted:	28	May	2026
Published:	01	June	2026

1- Introduction

Hydrogen-based energy systems are gaining relevance as power sectors move toward low-carbon generation and higher shares of variable renewables. Proton exchange membrane fuel cells (PEMFCs) have emerged as a promising solution for distributed generation, transportation, and rural/agricultural electrification because they can deliver high-efficiency electricity with reduced local emissions [1–3]. PEMFCs deployments frequently involve fast load variations and operating constraints. Therefore, control and energy-management designs require dynamic models that remain reliable beyond nominal operating points [4].

High-fidelity PEMFC models capture electrochemical, thermal, and mass-transport phenomena with strong physical interpretability, requiring many parameters and detailed sub-models, which complicates calibration and limits their use in real-time control and optimization [4]. For control-oriented studies, reduced-order and subsystem-level representations have therefore been explored to balance accuracy and computational cost, including non-parametric reduced-order modeling approaches and system-level simulations that preserve key transients for supervisory and

* **CONTACT**: edubenav@espol.edu.ec

DOI: https://doi.org/10.28991/ESJ-2026-010-03-01

embedded applications [5, 6]. In parallel, balance-of-plant air-supply dynamics and their coupling with stack voltage and power have been modeled to support controller development under realistic actuator limits [7]. Parameter identification studies further indicate that compact structures can preserve transient accuracy when their parameters are validated under representative excitation and operating variability [8].

Current investigations reinforce the need for application-ready dynamic models across energy systems [9]. Jenei et al. [10] discussed system-integration pressures at scale during Europe's renewable transition, underscoring how variability and operational constraints propagate into planning and operational decisions. Naidu et al. [11] investigated intelligent control for grid-connected PV systems, highlighting tracking and voltage regulation under fluctuating conditions through dynamic representations that remain reliable beyond nominal operating regimes. In agricultural deployments, Capcha-Ochoa et al. [12] and Yauri et al. [13] demonstrated, through solar-powered IoT irrigation and crop-monitoring applications, that supervisory actions must be robust to intermittent generation and demand variations in real-world installations. Thermal limitations were also emphasized by Oyewola et al. [14], whose research on battery thermal management showed that thermo-fluid operating constraints directly influence feasible control strategies and safety margins. Within PEMFC research, recent contributions on mechanistic multiphysics optimization of catalyst layers have highlighted the value of physically interpretable descriptions of internal transport and reaction phenomena [15]. In parallel, recent data-driven studies on voltage prediction under load transients indicate that practical models should be compact, control-oriented, and validated under excitation and disturbance conditions representative of closed-loop operation [16].

Despite this progress, the literature lacks a unified benchmark comparing CRA-based non-parametric estimation, low-order parametric structures, and grey-box state-space models under consistent excitation and validation protocols [6, 7]. This gap is particularly evident when extending analysis from SISO to MIMO configurations, where reactant-flow interactions and balance-of-plant coupling must be explicitly addressed. Additionally, the model choice directly affects prediction horizon, sensitivity to disturbances and constraints, and ultimately closed-loop performance when controllers must regulate voltage/power under fast demand changes and bounded actuation [8, 16]. Prior studies rarely link model selection to short- versus long-horizon predictive behavior under comparable excitation and validation protocols, which is essential for robust control and energy-management design. From a system identification standpoint, these requirements motivate a workflow that combines informative excitation, consistent validation, and model-structure comparison using both non-parametric and parametric-structured approaches [17, 18].

In this article we present a hybrid identification workflow using simulation data from a nonlinear PEMFC model implemented in MATLAB/Simulink. The plant is discretized and excited with multisine signals; correlation-based response analysis is used to obtain non-parametric dynamics, which are then benchmarked against low-order parametric structures (ARX, ARMAX, OE, BJ, and FIR) and a grey-box state-space model using a unified validation protocol in both SISO and MIMO settings [17, 18]. The main contributions are: (i) a reproducible multisine/CRA non-parametric identification pipeline for a discretized nonlinear PEMFC testbed; (ii) a unified comparison against standard low-order parametric structures and a grey-box state-space model under consistent validation criteria; (iii) an SISO-to-MIMO assessment that accounts for reactant-flow interactions; and (iv) practical guidance on selecting compact, validated models for control and energy-management studies.

The remainder of this paper is organized as follows: Section 2 summarizes the identification fundamentals and model structures; Section 3 details the data-generation procedure, excitation design, and validation protocol; Section 4 presents the hybrid identification methodology; Section 5 reports and discusses the comparative results ; and Section 6 concludes the paper and outlines implications for PEMFC control and energy-management applications.

2- Theoretical Foundations of PEMFC and System Identification

2-1- PEMFC Dynamics

Proton Exchange Membrane Fuel Cells (PEMFCs) convert chemical energy into electrical energy through electrochemical reactions between hydrogen and oxygen across a proton-conducting membrane. The theoretical reversible potential E_0 sets the thermodynamic limit, while the actual voltage decreases due to activation, ohmic, and concentration losses that determine the cell's dynamic behavior [4]. For control-oriented studies, reduced-order and system-level simulations have been explored to retain relevant transients at manageable complexity, including projection-based reduced-order modeling and stack-to-vehicle simulations [5, 6], and balance-of-plant coupling has been modeled to capture air-supply effects under realistic actuator limits [7]. The cell voltage can be expressed as:

$$V_{\text{cell}} = E_{\text{Nernst}} - \eta_{\text{act}} - \eta_{\text{ohmic}} - \eta_{\text{conc}} \tag{1}$$

where the Nernst voltage is:

$$E_{\text{Nernst}} = E_0 + \frac{RT}{2F}\ln\left(\frac{P_{H_2}\sqrt{P_{O_2}}}{P_{\text{ref}}}\right) \tag{2}$$

and the main loss terms are;

$$\eta_{\text{act}} = \frac{RT}{\alpha F} ln\left(\frac{i}{i_0}\right),\ \eta_{\text{ohmic}} = iR_{\text{int}},\ \eta_{\text{conc}} = \frac{RT}{F} ln\left(1-\frac{i}{i_{\text{lim}}}\right) \quad (3)$$

Activation losses η_{act} result from the energy barrier required for the electrochemical reaction to occur, whereas ohmic losses η_{ohmic} correspond to the resistive voltage drop through the membrane and electrodes. Concentration losses η_{conc} appear at high current densities when the reactant diffusion rate becomes insufficient [4, 5].

State variables include the cell voltage V_{cell}, current density i, and reactant partial pressures $\left(P_{H_2}, P_{O_2}\right)$. Temperature T is assumed constant (isothermal operation), and relative humidity (RH) is treated as fixed to sustain proton conductivity. Physical constants and parameters are: R(universal gas constant, $8.314\ \text{J/(mol. K)}$), F(Faraday constant, $96485\ \text{/mol}$), the charge-transfer coefficient α, the exchange current density i_0, the limiting current density i_{lim}, the internal ohmic resistance R_{int}, the reference pressure P_{ref} (typically 1 atm), and the reversible potential at reference conditions E_0. Units must be used consistently (e.g., pressure in atm, T in K, i in A/m² or A/cm², R_{int} in Ω) to ensure correct scaling of V_{cell} [4, 8].

This dynamic representation captures the transient coupling between electrochemical kinetics, gas diffusion, and electrical load, forming the basis for subsequent parametric and non-parametric identification. It enables realistic prediction of voltage and current responses under varying load conditions [6, 7].

2-2- Non-Parametric Identification

Non-parametric identification determines the dynamic behavior of the PEMFC without assuming a predefined model structure, focusing on the estimation of its impulse response and frequency response from simulated input–output data. The objective is to extract key dynamic features such as time constants, dominant poles, and gain, which characterize the voltage response under load variations [17, 18].

The correlation-based response analysis (CRA) method estimates the linear dynamic relationship between the input $u(t)$ (hydrogen flow rate) and the output $y(t)$ (cell voltage) through the cross-correlation function:

$$\varphi_{uy}(\tau) = \int_{-\infty}^{\infty} u(t)\, y(t+\tau)\, dt \quad (4)$$

where, $\varphi_{uy}(\tau)$ quantifies how changes in the excitation signal influence the cell voltage over time. The impulse response of the system is obtained by deconvolving $\varphi_{uy}(\tau)$, which yields the discrete-time impulse coefficients $g(k)$ [19, 20]:

$$g(k) = \mathcal{F}^{-1}\left\{\frac{\Phi_{uy}(j\omega)}{\Phi_{uu}(j\omega)}\right\} \quad (5)$$

where, $\Phi_{uy}(j\omega)$ and $\Phi_{uu}(j\omega)$ are the cross- and auto-spectral densities of the input–output signals, respectively; ω is the angular frequency (rad· s^{-1}), $j = \sqrt{-1}$, $\mathcal{F}^{-1}\{\cdot\}$ denotes the inverse Fourier transform, and $g(k)$ is the discrete-time impulse-response coefficient at lag k (with sampling time T_s) [19]. These coefficients represent the system's memory of past inputs and allow comparison with parametric models such as ARX, ARMAX, and Box–Jenkins, later discussed in the next subsection.

The analysis was performed using simulation data generated in MATLAB/Simulink under controlled multisine excitations that cover the frequency range of interest [20–22]. This non-parametric stage provides a reliable baseline for subsequent grey-box tuning and parametric identification [17, 18].

2-3- Parametric Identification

In the parametric identification stage, explicit mathematical models are fitted to the PEMFC input–output data to represent the dynamic relationship between hydrogen flow $u(t)$ and cell voltage $y(t)$. Each model structure introduces a different trade-off between accuracy and complexity, enabling a comparative assessment of how well the dynamics are captured [17, 20].

The finite impulse response (FIR) model directly represents the impulse response as a finite sequence of coefficients h_i:

$$y(t) = \sum_{i=1}^{n} h_i\ u(t-i) + e(t) \quad (6)$$

where, h_i are FIR impulse-response coefficients, n is the FIR order (number of coefficients), and $e(t)$ is the residual (prediction error) sequence. Although simple, the FIR model provides a baseline for locating dominant dynamic modes and assessing transport delays.

The auto-regressive with exogenous input (ARX) model introduces feedback by expressing the output as a combination of past outputs and past inputs:

$$A(q^{-1})\, y(t) = B(q^{-1})\, u(t) + e(t) \quad (7)$$

where, $A(q^{-1})$ and $B(q^{-1})$ are polynomials in the backshift operator q^{-1} which denotes the backward shift (one-sample delay) operator, i.e., $q^{-1}x(t) = x(t-1)$. This structure efficiently captures transient effects and is computationally attractive for preliminary fitting [17].

The ARMAX model extends ARX by incorporating a moving-average term $C(q^{-1})$, which improves noise modeling and prediction quality:

$$A(q^{-1})\,y(t) = B(q^{-1})\,u(t) + C(q^{-1})\,e(t) \tag{8}$$

The Box–Jenkins (BJ) model separates deterministic and stochastic dynamics by using distinct denominators for the process and noise:

$$y(t) = \frac{B(q^{-1})}{F(q^{-1})}u(t) + \frac{C(q^{-1})}{D(q^{-1})}e(t) \tag{9}$$

Finally, the output-error (OE) model minimizes the output residuals by fitting only the deterministic dynamics, assuming negligible noise feedback:

$$y(t) = \frac{B(q^{-1})}{F(q^{-1})}u(t) + e(t) \tag{10}$$

The identification of these parametric structures was carried out using the System Identification Toolbox in MATLAB, based on the simulated input–output datasets [21]. Each model was tuned to match the voltage transient response obtained from the PEMFC dynamic block, providing a comparative evaluation of model complexity versus predictive accuracy [17, 23].

2-4- Model Validation

Model validation verifies that the identified structure reproduces the PEMFC voltage behavior with sufficient accuracy. The residual $e(t)$ is defined as the difference between the measured output $y(t)$(cell voltage from simulation or experiment) and the model-predicted output $\hat{y}(t)$ [17, 18]:

$$e(t) = y(t) - \hat{y}(t) \tag{11}$$

A valid model yields small, uncorrelated residuals that behave as white noise. The cross-correlation between input $u(t)$and residual $e(t)$is also evaluated; ideally, it is close to zero for all lags [17, 19], confirming that no significant dynamic information remains unmodeled:

$$\varphi_{ue}(\tau) = \int_{-\infty}^{\infty} u(t)\,e(t+\tau)\,dt \tag{12}$$

These criteria confirm that the chosen parametric and non-parametric structures capture the essential PEMFC dynamics before advancing to model discretization and SISO/MIMO formulations.

3- Dynamic Model Derivation and Discretization

The PEMFC plant relates the hydrogen and oxygen flow rates to the cell voltage and power output, governed by electrochemical and thermal equations. The total cell voltage can be written as:

$$V_{\text{cell}} = E_{\text{Nernst}} - (\eta_{\text{act}} + \eta_{\text{ohmic}} + \eta_{\text{conc}}) + v_{\text{noise}} \tag{13}$$

where, E_{Nernst} denotes the reversible (ideal) voltage from the Nernst equation (V), and v_{noise} represents a low-amplitude filtered Gaussian measurement-noise term (V) (kept below 1% of the nominal voltage). The terms η_{act}, η_{ohmic}, and η_{conc} are the activation, ohmic, and concentration overpotentials (V), respectively, accounting for electrochemical kinetics, internal resistive losses, and mass-transport limitations. This term V_{cell} provides a controlled representation of measurement uncertainty and natural fluctuations in cell voltage acquisition [4, 19].

The voltage losses depend on the current $i(t)$, which leads to a first-order dynamic model:

$$\tau_s \frac{dV_{\text{cell}}}{dt} + V_{\text{cell}} = V_{\text{ideal}} - \eta_{\text{total}} \tag{14}$$

where, τ_s is an equivalent dominant time constant representing the aggregated PEMFC voltage dynamics around the operating point (s), V_{ideal} is the ideal voltage term (V), and $\eta_{\text{total}} = \eta_{\text{act}} + \eta_{\text{ohmic}} + \eta_{\text{conc}}$ is the total voltage loss (V). The physical parameters, such as the exchange current density i_0, internal resistance R_{int} , and operating temperature T, are obtained from experimental characterization and electrochemical literature [4, 8].

Applying the Laplace transform to Equation 14 under linearity and zero initial conditions yields the general cell model in the frequency domain:

$$V(s) = E(s) - \eta_{\text{ohmic}}(s) - \eta_{\text{act}}(s) - \eta_{\text{conc}}(s) \tag{15}$$

where, $E(s)$corresponds to the ideal voltage and each $\eta(s)$ represents a loss component in the Laplace domain. This transformation procedure is detailed in standard PEMFC modeling references [4, 5], where the approximations used in dynamic PEMFC simulation are justified. Typical parameters employed in the simulation are $F = 96485$ C/mol, $T = 353$ K, $P_{H_2} = P_{O_2} = 1$ atm, $R_{\text{int}} = 0.01\ \Omega$ and $i_0 = 5$ mA/cm^2 [4, 8].

The continuous model was discretized using the Tustin method (bilinear transform) [24], which preserves stability and approximates the continuous dynamics when transitioning to the discrete domain. In this method, the Laplace variable $s$is replaced by:

$$s = \frac{2}{T_s}\,\frac{1 - z^{-1}}{1 + z^{-1}} \tag{16}$$

where, T_s is the sampling time (s), z^{-1} is the one-sample delay operator, and the bilinear (Tustin) mapping is used to obtain a discrete-time representation suitable for identification and validation. This approximation provides an accurate digital representation of the continuous system, preserving the frequency-domain response. The resulting discrete transfer function is:

$$G_{\text{total}}(z) = \frac{0.0134z^2 + 0.01579z + 0.002362}{z^2 - 1.505z + 0.5429} \tag{17}$$

where, $G_{\text{total}}(z)$ represents the discrete transfer function of the system and $z$is the complex variable of the z-transform. For numerical validation and model reduction, this discrete model was compared with the reduced-order approach presented in (14), showing a consistent dynamic response suitable for real-time simulation.

In the SISO configuration, a single input $u(t)$(hydrogen flow) and a single output $y(t)$ (cell voltage) are considered, as defined by (15). In the MIMO configuration, the model includes two inputs and two outputs, expressed as:

$$\begin{bmatrix} Y_1 \\ Y_2 \end{bmatrix} = \begin{bmatrix} G_{11}(z) & G_{12}(z) \\ G_{21}(z) & G_{22}(z) \end{bmatrix} \begin{bmatrix} U_1 \\ U_2 \end{bmatrix} + \begin{bmatrix} W_1 \\ W_2 \end{bmatrix} \tag{18}$$

where, $U_1$and U_2 represent the hydrogen and oxygen (air) flow rates, respectively, while Y_1 corresponds to the cell voltage and Y_2 to the electrical power. Each $G_{ij}(z)$ denotes the discrete-time transfer function of the corresponding input–output path, estimated from the multisine-excited data using the considered identification structures (ARX/ARMAX/OE/BJ/FIR) and the sampling time $T_s = 0.1$ s. The effective model order and dynamics are therefore determined by the selected structure and tuning rather than assumed a priori. The terms W_i represent filtered measurement perturbations. The structural representation of the SISO and MIMO configurations used for identification and validation is shown in Figure 1 [17, 18, 20].

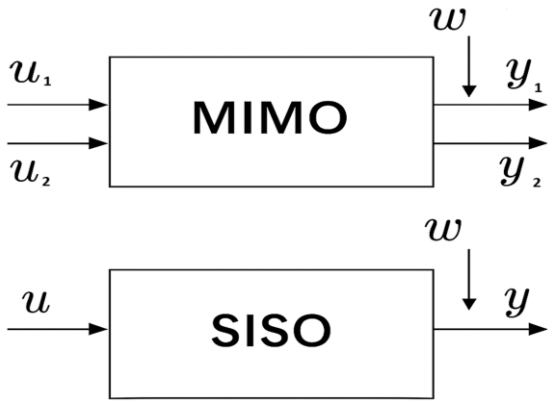

Figure 1. Simplified SISO and MIMO models used for system identification and validation

The discrete PEMFC model provides the basis for dynamic analysis. A non-parametric identification is then applied to validate this structure and to derive the system behavior directly from input–output data.

4- Identification Methodology

Figure 2 illustrates the proposed identification workflow, comprising: (i) operating-point definition including temperature (T), pressure (P), load current (i), and relative humidity (RH) , (ii) multisine excitation design within a target frequency band $f \in [f_{\min}, f_{\max}]$using N harmonics with amplitude scaling A_k to ensure persistent excitation while preserving physically admissible inputs, (iii) data acquisition and pre-processing (*e.g.*, filtering, detrending, and segmentation), (iv) CRA-based non-parametric baseline estimation (FRF/impulse response), (v) subsequent discrete-time parametric identification (ARX, ARMAX, OE, BJ, FIR), (vi) grey-box state-space modeling, and (vii) model selection and validation using Fit%, AIC, and residual/time-domain tests.

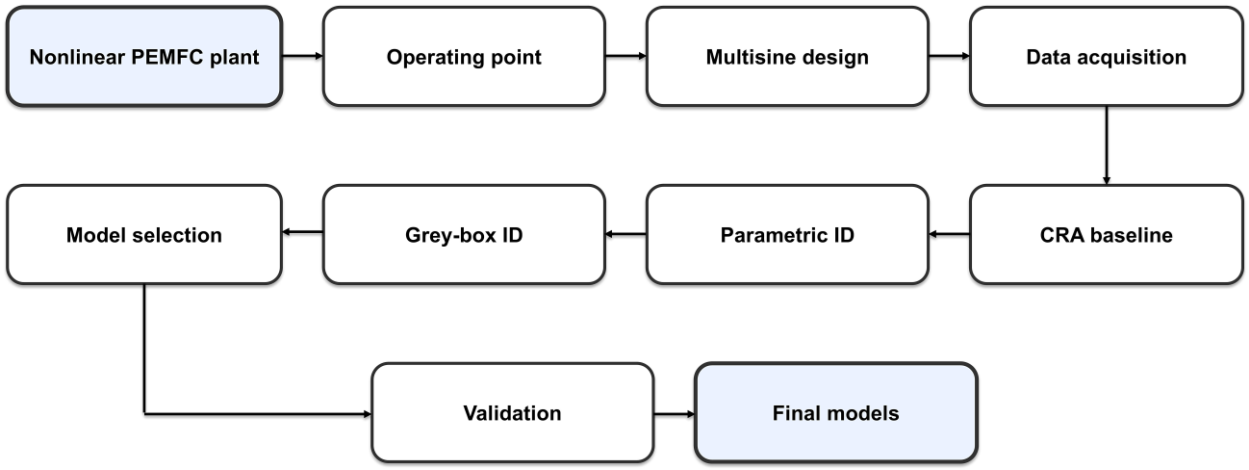

Figure 2. Methodological workflow for sequential hybrid identification of the nonlinear PEMFC plant

4-1- Stochastic Noise Characterization and Signal Integrity

To emulate measurement uncertainty in the simulation-based identification setup, the output signals used for CRA and subsequent parametric estimation are treated as noisy measurements. As shown in Figure 3, the measured output is modeled as:

$$y[k] = G(q)\,u[k] + w[k] \tag{19}$$

where, $G(q)$ denotes the discrete-time input–output mapping (with q^{-1} the unit-delay operator) and $w[k]$ is an additive stochastic disturbance at the measurement channel. In this work, $w[k]$is implemented in Simulink as band-limited additive white Gaussian noise (AWGN) with zero mean and variance σ^2, i.e.,

$$w[k] \sim \mathcal{N}(0, \sigma^2) \tag{20}$$

Although the Simulink noise block is band-limited, its power spectral density is approximately flat within the identification band, providing a conservative broadband perturbation that stresses the estimators over the same spectral region where the system dynamics are inferred. This additive measurement-noise assumption is consistent with standard system-identification formulations [17, 21]. Although Figure 3 uses continuous-time notation for clarity, all signals are sampled with T_s and q^{-1} denotes a one-sample delay.

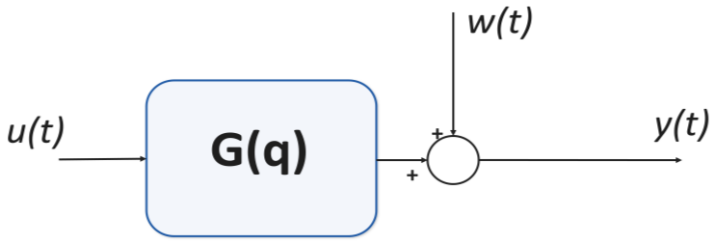

Figure 3. Measurement model adopted for identification

4-2- Non-Parametric Identification of the SISO and MIMO System

Non-parametric identification was applied to characterize the dynamic behavior of the PEM fuel cell (PEMFC) in both SISO and MIMO configurations. This approach, widely used in control and system identification, estimates system dynamics directly from input–output data without assuming a predefined model structure. In this work, it is used to analyze transient and steady-state responses and to support the subsequent parametric and grey-box modeling stages [19, 20].

The procedure combines three elements:

- Multisine excitation signals with suitable amplitude and frequency content.
- Correlation-based Response Analysis (CRA) for impulse- and step-response estimation.
- Validation through comparison with simulated validation data.

To ensure sufficient excitation of the plant dynamics, multisine signals were generated for both SISO and MIMO configurations following standard identification guidelines [17, 20, 22]. These signals uniformly cover the relevant frequency range while mitigating noise effects. In the MIMO setup, the two input excitations correspond to perturbations in hydrogen and air flow rates applied to the PEMFC model. The excitation is given by:

$$u(t) = \sum_{k=1}^{N} A_k \sin(2\pi f_k t + \phi_k) \quad (21)$$

where, N is the number of harmonics, A_k is the amplitude of the k-th sinusoidal component, f_k is its frequency (Hz), and ϕ_k is its phase (rad). The excitation band is defined by $f_k \in [f_{\min}, f_{\max}]$, with $f_{\min}$ and $f_{\max}$ denoting the minimum and maximum excitation frequencies, respectively. Using CRA, impulse and step responses are estimated from the cross-correlation between the excitation signals and the measured outputs. These non-parametric responses serve as a reference to assess the quality of the later parametric and grey-box models and to identify the dominant time scales of the PEMFC dynamics [19, 22].

The multisine excitation was designed to ensure persistent excitation over the dynamic range of interest while keeping bounded perturbations around the selected operating point. With sampling time $T_s = 0.1$ s and sequence length $N_s = 616$, the excitation period is $T_p = N_s T_s = 61.6$s, which yields the fundamental frequency $f_0 = 1/T_p = 0.01623$Hz (i.e., $\omega_0 = 2\pi f_0 = 0.1020$rad/s). Using $N_h = 5$ excited harmonics ($k = 1, \ldots, 5$), the identification band becomes $[\omega_{\min}, \omega_{\max}] = [\omega_0, N_h\omega_0] = [0.1020, 0.5100]$rad/s. The hydrogen input is applied as a normalized deviation $\Delta u_{H_2}(t)$(p.u.) to enforce bounded excitation without altering the designed spectral content. The resulting time-domain realization is shown in Figure 4, while Figure 5 confirms the corresponding discrete harmonic lines within the selected band, with $\omega_{\min}$ and $\omega_{\max}$ indicated for clarity.

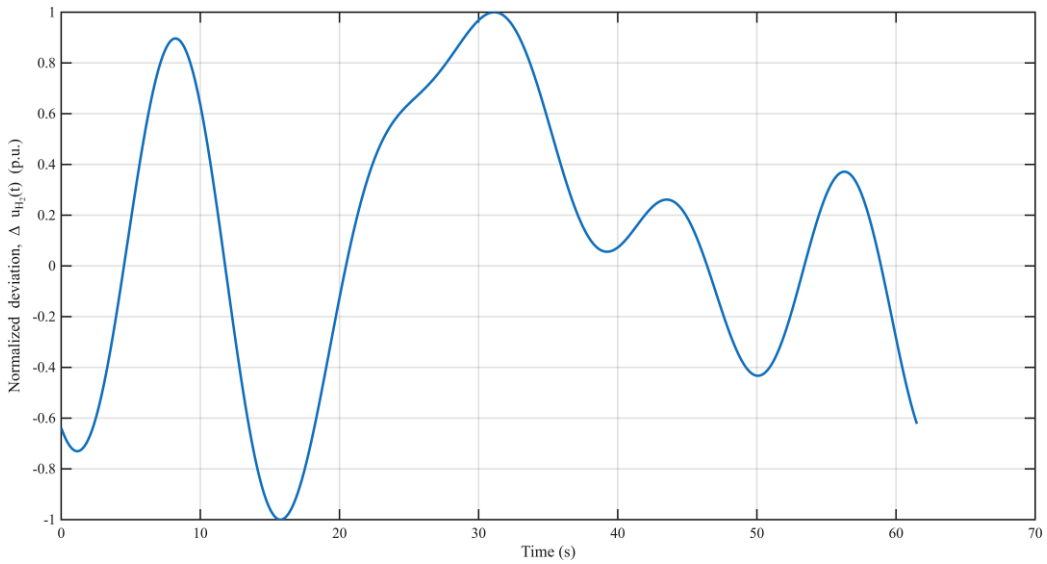

Figure 4. Hydrogen multisine input (normalized deviation, p.u.)

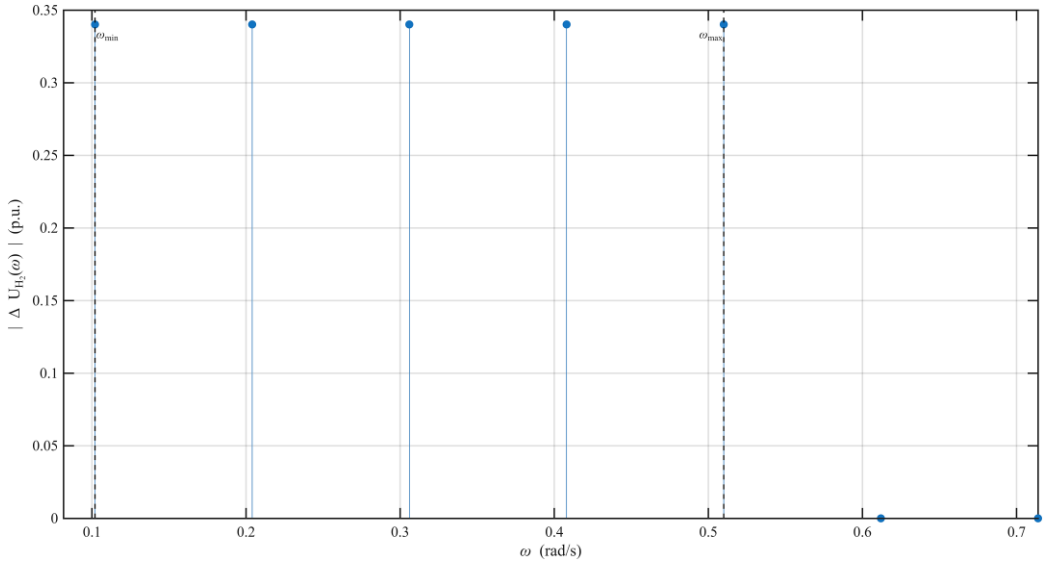

Figure 5. Hydrogen multisine excitation spectrum (discrete harmonics, p.u.)

For the MIMO case, an analogous multisine design (same sampling and harmonic-structure principles) was applied to the second input channel (oxygen flow), ensuring comparable broadband excitation across both inputs.

4-3- Parametric Identification of the System

Parametric identification aims to obtain compact mathematical models that accurately represent the dynamic behavior of the PEMFC system based on input–output data. The model parameters are estimated by minimizing the discrepancy between measured and simulated outputs, seeking a balance between accuracy and structural simplicity. Both SISO and MIMO configurations are considered to analyze individual responses and the coupling effects among variables.

The candidate structures include FIR, ARX, ARMAX, Box–Jenkins (BJ), and Output Error (OE) models. For each configuration, several model orders are tested using MATLAB's System Identification Toolbox, and the best models are selected according to the criteria described below [17, 21].

4-4- Model Selection Criteria

The selection of candidate parametric models is guided by a combined accuracy–parsimony criterion. Specifically, we employ the fit percentage (Fit%) to quantify time-domain agreement, and two information criteria—Akaike Information Criterion (AIC) and Bayesian Information Criterion (BIC)—to penalize unnecessary model complexity and reduce overfitting risk. This combination is widely recommended for control-oriented identification, where compact models with strong generalization are preferred over highly parameterized structures [9, 17, 23].

The AIC is a statistical measure that evaluates the trade-off between model accuracy and complexity, penalizing the excessive use of parameters. It is defined as:

$$\mathrm{AIC} = N\ln\left(\frac{\mathrm{RSS}}{N}\right) + 2p \tag{22}$$

where, N is the number of samples, $\mathrm{RSS} = \sum_{k=1}^{N} e^2(k)$ is the residual sum of squares, and p is the number of model parameters. Lower AIC values indicate a more efficient representation of the system and a reduced risk of overfitting.

To complement AIC, we also compute BIC, which applies a stronger penalty as the dataset size grows. This property is useful to discourage over-parameterized models when multiple candidates achieve similar fits. BIC is defined as:

$$BIC = N\ln\left(\frac{\mathrm{RSS}}{N}\right) + pln(N) \tag{23}$$

Lower BIC values indicate better expected generalization under a stricter complexity penalty than AIC [23].

The fit percentage (Fit%) quantifies the agreement between the measured and simulated outputs. It is computed as:

$$\mathrm{Fit}(\%) = \left(1 - \frac{\|y-\hat{y}\|}{\|y-\bar{y}\|}\right) \times 100 \tag{24}$$

where, y is the measured output, $\hat{y}$ is the model output, and $\bar{y}$ is the mean of y. Values close to 100% indicate that the model reproduces the system behavior with high accuracy.

Values closer to 100% indicate high time-domain accuracy. Importantly, Fit% alone is not sufficient to guarantee model validity; therefore, the final selection is supported by residual diagnostics (whiteness and independence tests) described next [17, 19].

After ranking candidates using Fit%, AIC, and BIC, residual analysis is performed to verify that the model has captured the predictable dynamics and that the remaining error behaves as approximately white noise. Residual diagnostics are a standard requirement in system identification because a high Fit% may still coexist with structured residuals (i.e., unmodeled dynamics), which can bias subsequent interpretation and control design [17, 19]. Let the residual sequence be defined as:

$$e(k) = y(k) - \hat{y}(k) \tag{25}$$

where, y(k) denotes the measured (or simulated plant) output at sample k, while $\hat{y}$(k) is the model output obtained by simulating (or predicting) the identified model using the same input sequence. The residual e(k) therefore represents the portion of the output that is not explained by the model dynamics. A satisfactory model should concentrate all predictable, input-driven behavior in $\hat{y}$(k), leaving e(k) as an unpredictable component dominated by noise and unmodeled disturbances. The residual autocorrelation function is evaluated to check whether correlation remains at nonzero lags:

$$\hat{r}_{ee}(\tau) = \frac{1}{N}\sum_{t=1}^{N-\tau} e(t)\, e(t+\tau) \tag{26}$$

where, N is the total number of samples in the validation record and $\tau$is the integer lag ($\tau = 0,1, \ldots$). The term $e(k)$ is the residual defined in (25). If the model captures the relevant dynamics adequately, the residual should be approximately white; therefore, $\hat{r}_{ee}(\tau)$ should be close to zero for all nonzero lags ($\tau \neq 0$). Persistent nonzero autocorrelation indicates remaining structured dynamics not captured by the model.

For a satisfactory model, $\hat{r}_{ee}(\tau)$ should be close to zero for $\tau \neq 0$ and lie within approximate 95% confidence bounds:

$$\text{bounds } (95\%) \approx \pm \frac{1.96}{\sqrt{N}} \tag{27}$$

This provides an approximate 95% confidence interval commonly used to assess whether sample correlation values are statistically distinguishable from zero under the assumption of white, independent residuals. Here, $N$is the number of samples used to compute the correlation. In practice, both $\hat{r}_{ee}(\tau)$ and $\hat{r}_{ue}(\tau)$(defined below) are compared against these bounds: correlations remaining within $\pm 1.96/\sqrt{N}$ are interpreted as consistent with whiteness/independence, while repeated excursions outside the bounds suggest model inadequacy or remaining input-driven structure. Residuals that remain inside the confidence bounds indicate that the modeling error is largely uncorrelated in time (white), supporting the adequacy of the identified dynamics. In addition, we verify that residuals are not correlated with past inputs, which would indicate that part of the input-driven dynamics is still unmodeled (i.e., the residual is "explainable" by the input). The normalized cross-correlation is computed as:

$$r_{ue}(\tau) = \frac{\sum_{k=1}^{N-\tau} u(k)\, e(k+\tau)}{\sqrt{\left(\sum_{k=1}^{N} u^2(k)\right)\left(\sum_{k=1}^{N} e^2(k)\right)}} \tag{28}$$

where, $u(k)$ is the input sequence (e.g., the normalized reactant-flow command used for excitation), $e(k)$ is the residual from (25), $N$is the record length, and τ is the lag. This test verifies that the residual is not explainable by past inputs: for a well-identified model, $r_{ue}(\tau)$ should be close to zero (and remain within the 95% bounds of (27)) for the inspected lags. Significant nonzero values of $r_{ue}(\tau)$ indicate that the model has not fully captured the input–output dynamics, and that part of the input-driven behavior is still present in the residual [17, 19].

4-5- PEMFC System Identification Using a Grey-Box Model

Grey-box modeling is employed to represent the PEMFC dynamics by combining physical electrochemical knowledge with identification from data. The objective is to obtain a model that captures transient and steady-state voltage variations while maintaining physical interpretability of the parameters. The proposed structure integrates the main polarization phenomena (activation, ohmic, and concentration losses) into a simplified dynamic formulation.

Parameter estimation is carried out using the prediction-error method with iterative least-squares optimization, using hydrogen and oxygen flow rates U_1, U_2 as inputs and stack voltage and power Y_1, Y_2 as outputs. Under this approach, the PEMFC is represented in continuous state-space form [18]:

$$\dot{X} = AX + BU,\ Y = CX + DU \tag{29}$$

where, $X \in \mathbb{R}^{n_x}$ is the state vector, $U = [U_1\ U_2]^T$ is the input vector (reactant flow rates), and $Y = [Y_1\ Y_2]^T$ is the output vector (stack voltage and power), A, B, C, and D are the state, input, output, and feedthrough matrices that encode the dynamic relationships between reactant flows and electrical outputs. These matrices are tuned using MATLAB's Identification Toolbox to match simulated validation data and to retain consistency with the underlying electrochemical model [9, 21].

At this point, the complete identification framework is established: starting from the PEMFC dynamic model and its discretization, through non-parametric CRA analysis, to parametric and grey-box structures with clearly defined validation criteria. The next section presents numerical results and discussion.

5- Results and Discussion

This section presents the results obtained with the proposed identification framework. First, the non-parametric behavior of the PEMFC is characterized using CRA, yielding impulse and step responses for both SISO and MIMO configurations. These responses are used to validate the excitation design and to identify the dominant time scales of dynamics. Then, the performance of the parametric and grey-box models is assessed by comparing their ability to reproduce the non-parametric responses and the original input–output data in both SISO and MIMO settings.

5-1- Non-Parametric Identification (CRA)

The CRA (Correlation-based Response Analysis) is first employed to obtain a non-parametric baseline of the PEMFC dynamics prior to parametric and grey-box modeling. CRA estimates the discrete-time impulse response by combining input prewhitening with prewhitened cross-correlation, which yields a consistent FIR-type description of the local input–

output mapping around the selected operating point. This step is used to (i) validate the excitation design, (ii) identify dominant time scales, and (iii) guide the structure selection of subsequent parametric models [17].

Figure 6 reports the CRA-estimated impulse response for the hydrogen-to-voltage channel (U1 → Y1), together with its unit-step equivalent response obtained by cumulative summation of the impulse response. The impulse response concentrates most of its energy in the early samples and decays rapidly toward zero, indicating a stable, finite-memory behavior dominated by a main slow mode with a faster parasitic component. The corresponding step response reaches its steady-state region within a short transient and exhibits only a mild peak before settling, which supports the use of low-order control-oriented structures (e.g., first-order plus a fast mode) for local modeling. This behavior is consistent with small-signal PEMFC voltage dynamics commonly reported around fixed operating conditions. [4, 8].

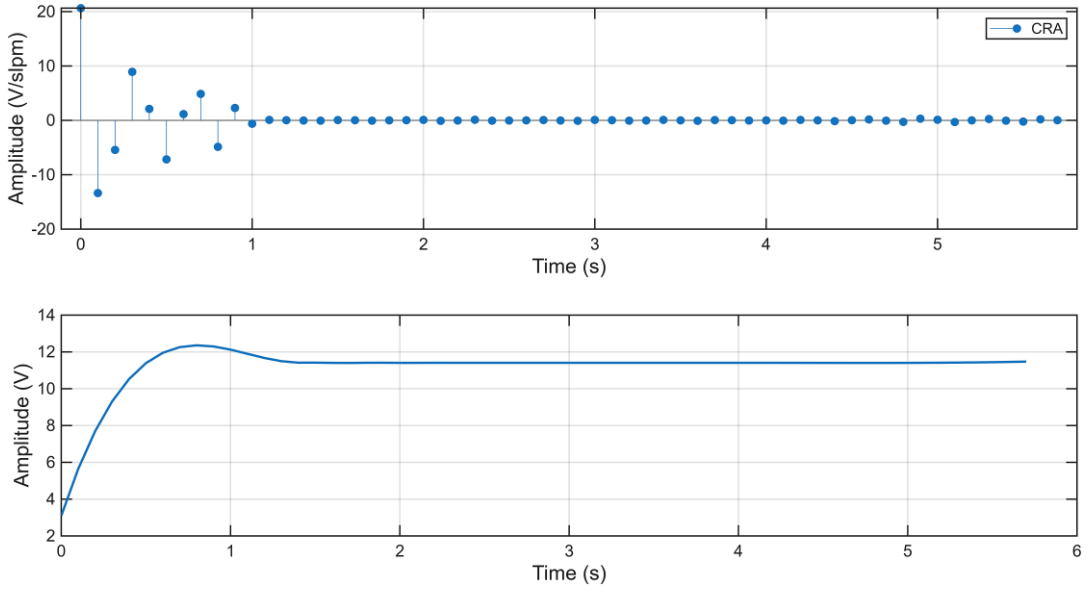

Figure 6. CRA non-parametric responses for the SISO channel

To verify that the obtained FIR baseline is not only qualitatively plausible but also predictive, Figure 7 compares the CRA-reconstructed step response against the step response obtained directly from the simulated plant data under the same input change. The two curves show close agreement in rise behavior, peak region, and steady-state level, while small discrepancies are mainly confined to the initial transient where unmodeled nonlinear effects and stochastic contamination have the strongest influence. Overall, this comparison confirms that CRA provides a reliable non-parametric description of the local SISO dynamics and can be used as a reference for subsequent parametric/grey-box identification.

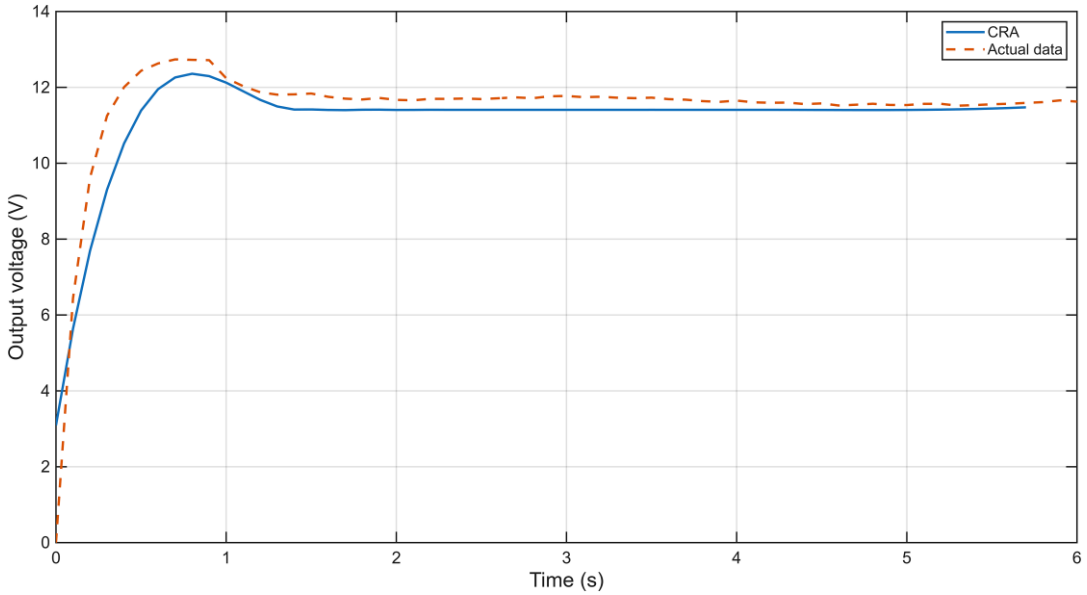

Figure 7. Validation of the CRA baseline in SISO: comparison between the CRA-reconstructed step response and the step response obtained from the simulated plant data for the same hydrogen input step

The CRA procedure was then applied to the MIMO dataset by analyzing each input–output channel. For conciseness, Figure 8 shows a representative channel (U2 → Y1), selected because it exhibits a clear causal correlation signature and a compact impulse response. The covariance plots of the prewhitened signals confirm that the whitening stage suppresses dominant correlations, while the prewhitened cross-correlation highlights the causal relationship (negligible correlation at negative lags and significant response at positive lags). The resulting CRA impulse response provides a non-parametric FIR estimate of the channel dynamics, enabling an interpretable characterization of dominant time scales and coupling strength. The remaining channels showed analogous causality patterns and comparable time-scale features, and thus U2 → Y1 is used here as a representative example to illustrate the CRA baseline in MIMO prior to parametric/grey-box fitting.

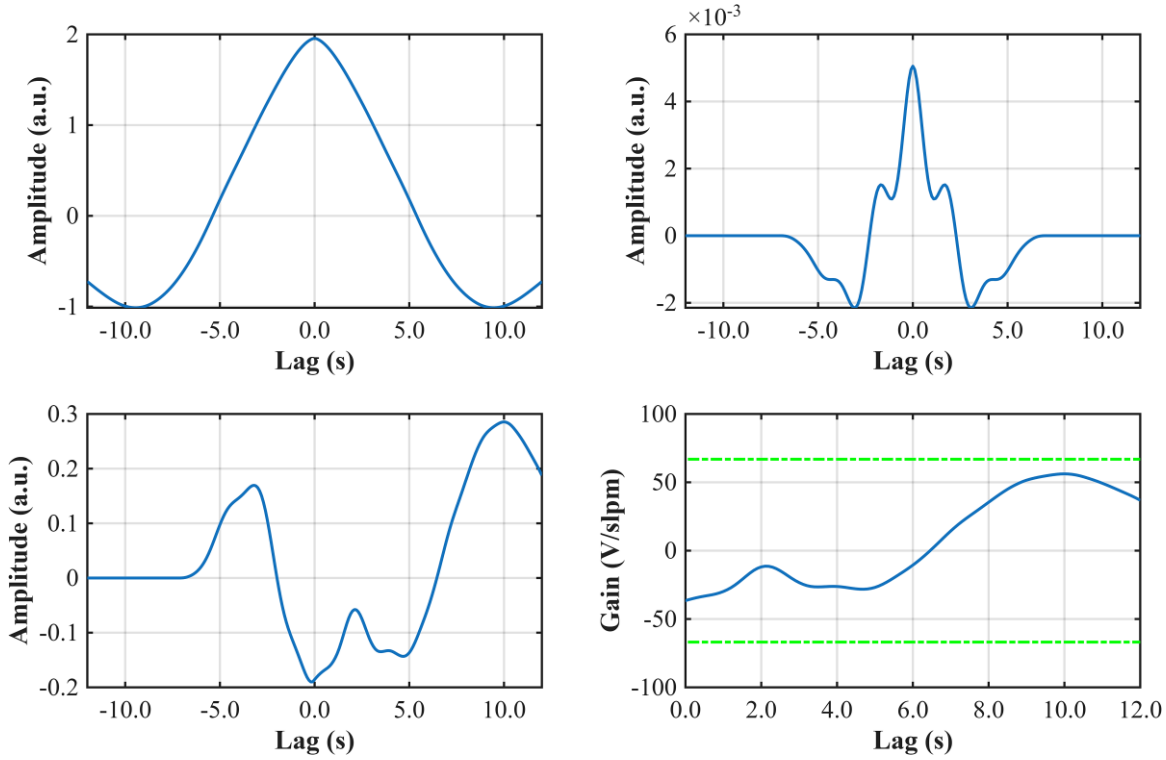

Figure 8. CRA correlation analysis for a representative MIMO channel (U2 → Y1). (a) Covariance of the prewhitened output signal. (b) Covariance of the prewhitened input signal. (c) Cross-correlation between the prewhitened input and output, highlighting the dominant lag structure. (d) CRA-based impulse response estimate (gain), which summarizes the dynamic mapping from U2 to Y1 under the selected excitation and operating point.

These results validate the effectiveness of the excitation strategy and the application of standard identification guidelines for PEMFC systems in both SISO and MIMO configurations.

5-2- Results of Parametric Identification for the SISO Configuration

In the SISO configuration, the hydrogen flow rate was considered as the input and the stack voltage as the output. Five discrete-time parametric structures (ARX, ARMAX, Box–Jenkins (BJ), Output-Error (OE), and FIR) were estimated using the same identification dataset and subsequently evaluated on an independent validation segment. The objective was to obtain a control-oriented model that balances prediction accuracy and parsimony.

Table 1 summarizes the model comparison in terms of: (i) Fit%, which quantifies time-domain agreement between measured and simulated outputs; (ii) AIC, which penalizes model complexity while rewarding goodness of fit; and (iii) BIC, which applies a stronger penalty to complexity and therefore tends to favor more parsimonious structures for large datasets. In addition, the number of estimated parameters (Npar) is included to provide a direct measure of structural complexity.

From Table 1, the BJ model achieves the highest Fit% (98.747%), indicating excellent reproduction of the measured output. However, this improvement comes at the cost of a larger parameterization (Npar = 8) and less favorable information criteria compared with the best-ranked candidates. In contrast, ARMAX yields a high Fit% (96.838%) while achieving the lowest AIC and BIC, which indicates the most efficient trade-off between accuracy

and complexity among the tested structures. The ARX model provides a Fit% close to ARMAX (96.407%) but requires a larger number of parameters in this configuration (Npar = 12) and is therefore less favored by AIC/BIC despite its strong time-domain fit. The OE model shows competitive Fit% (97.269%), yet its information criteria values are not as favorable as the top-ranked candidates, which suggests that its residual/noise characterization is not as efficient under the present dataset and operating-point conditions. Finally, the FIR model exhibits the lowest Fit% (84.086%), confirming that a short FIR structure is insufficient to capture the dominant PEMFC voltage dynamics in this identification scenario.

Table 1. Comparison of parametric models for SISO configuration

Model family	Npar	Fit [%]	AIC	BIC
ARMAX	6	96.838	-7134.700	-7108.200
Box–Jenkins (BJ)	8	98.747	-6818.800	-6783.400
ARX	12	96.407	-7121.900	-7068.900
Output-Error (OE)	4	97.269	-2123.400	-2105.700
FIR	2	84.086	44.215	53.062

Figure 9 compares the measured voltage trajectory against the simulated outputs obtained with the five identified model families. Overall, BJ, OE, ARX, and ARMAX reproduce the main waveform with very small deviation over the full horizon, confirming that the dominant linear dynamics around the selected operating point are well captured by these parametric structures. The agreement is particularly strong at the main extrema (e.g., the first positive peak and the subsequent negative trough), indicating that the models capture both the effective gain and the dominant time constant of the SISO PEMFC dynamics.

Nonetheless, Figure 9 also reveals subtle but relevant differences. The FIR model shows visibly larger discrepancies during faster transients and in regions where the signal curvature changes more abruptly, which is consistent with its limited memory length and lower Fit% in Table 1. Among the high-performing structures, BJ tends to track the measured waveform most tightly, whereas ARMAX and ARX offer a very similar match with slightly smoother behavior typically desirable for control-oriented usage where excessive flexibility may not generalize as well.

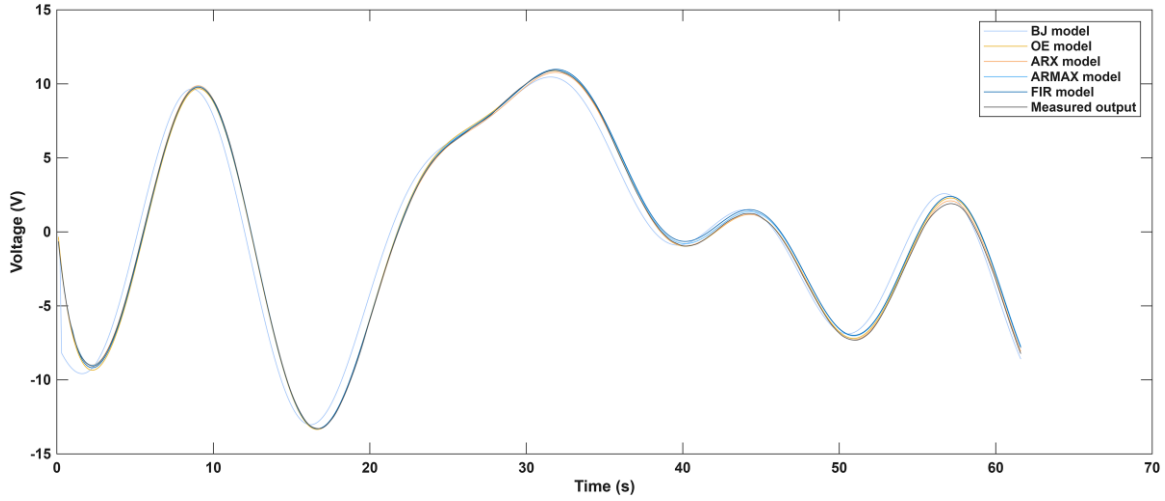

Figure 9. Comparison of SISO parametric model structures

Figure 10 summarizes the residual analysis for the SISO parametric models. In the upper panel (residual autocorrelation test), OE (yellow), BJ (orange), and FIR (light blue) exhibit peaks/segments that exceed the confidence bounds at non-zero lags, indicating non-white residuals (remaining temporal structure in the error). In contrast, ARX (blue) and ARMAX (dark blue) remain mostly within the bounds, suggesting a residual closer to white and thus less unmodeled dynamics in the prediction error for the evaluated validation data. In the lower panel (input–residual cross-correlation test), the curves stay within the confidence bounds for OE and BJ, while only the FIR model shows a clear violation. This pattern indicates that, for FIR, a non-negligible fraction of the output behavior is still explainable by the input, i.e., the input–output dynamics are under-modeled, consistent with its weaker overall performance.

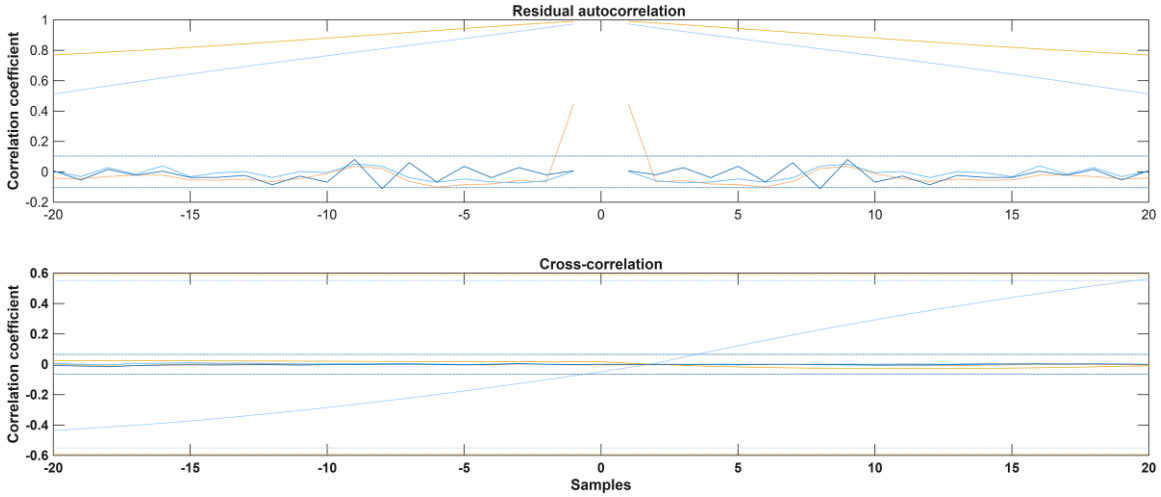

Figure 10. Residual diagnostics for SISO parametric models

5-3- Results in the MIMO Configuration

In the MIMO configuration, two inputs U_1 and U_2 affect two outputs Y_1 and Y_2, leading to coupled dynamics across the four input–output pathways ($U_1 \rightarrow Y_1$, $U_1 \rightarrow Y_2$, $U_2 \rightarrow Y_1$, $U_2 \rightarrow Y_2$). To provide a transparent and control-oriented assessment, the identified parametric candidates are reported and compared per channel, using the same validation protocol adopted in the SISO case. The evaluation emphasizes a balanced selection between prediction accuracy and parsimony, supported by information criteria and residual diagnostics.

Table 2 reports the top 3 parametric candidates retained for each MIMO input–output channel, together with the number of parameters (Npar), validation Fit%, and the information criteria AIC and BIC. The ranking combines: (i) Fit% on validation data as a time-domain accuracy indicator; and (ii) AIC and BIC, which penalize excessive parameterization and help prevent overfitting, thus favoring parsimonious structures when predictive performance is similar. For $U_1 \rightarrow Y_1$, ARMAX offers the most attractive accuracy–parsimony balance (high Fit% with a low-order structure, Npar = 6), while BJ achieves a comparable Fit% at a higher parameter count. For $U_1 \rightarrow Y_2$, the BJ structure clearly outperforms the other candidates in terms of Fit%, indicating that this pathway is more difficult to capture with compact ARX/ARMAX models under the current excitation and operating conditions. For $U_2 \rightarrow Y_1$, the leading structures exhibit uniformly high fits (≈99.4%), so parsimony becomes the main discriminator; in this case ARMAX achieves similar accuracy with fewer parameters (Npar = 8) than BJ and ARX (Npar = 14 and 16, respectively), while remaining competitive under AIC/BIC. Finally, for $U_2 \rightarrow Y_2$, Fit% values are also close (≈93%), and the preference is primarily guided by the complexity-penalized criteria; although ARX attains a marginally higher Fit%, BJ provides substantially lower AIC/BIC with fewer parameters, suggesting a more parsimonious representation for this channel. These quantitative indicators provide the basis for the detailed time-domain and residual discussions presented next for each channel.

Table 2. Comparison of parametric models for MIMO configuration

Configuration	Rank	Model	Npar	Fit (%)	AIC	BIC
U1 → Y1	1	ARMAX	6	97.85	-4389.8	-4363.3
U1 → Y1	2	BJ	8	97.23	-4375.8	-4340.5
U1 → Y1	3	OE	4	95.95	-1895.7	-1878.0
U1 → Y2	1	BJ	15	86.38	-3959.5	-3893.1
U1 → Y2	2	ARMAX	6	3.85	-3746.4	-3719.9
U1 → Y2	3	ARX	11	9.51	-3702.5	-3653.9
U2 → Y1	1	BJ	14	99.44	-3441.2	-3382.2
U2 → Y1	2	ARX	16	99.39	-3349.8	-3282.3
U2 → Y1	3	ARMAX	8	99.42	-3422.7	-3388.9
U2 → Y2	1	BJ	8	93.08	-4084.7	-4049.4
U2 → Y2	2	ARX	13	93.10	-4041.6	-3984.1
U2 → Y2	3	ARMAX	6	92.92	-4062.7	-4036.1

Figure 11 compares the measured voltage output Y_1 against the simulated responses obtained with the candidate parametric structures for the $U_1 \rightarrow Y_1$ pathway. Overall, the leading models reproduce the dominant waveform with small discrepancies, capturing the main extrema and the intermediate inflection regions. Consistent with Table 2, ARMAX provides the most accurate and stable tracking over the full validation horizon, closely matching the measured trajectory at the dominant peak and trough while maintaining smooth behavior around the mid-range oscillations. BJ achieves a similarly high-quality match over most of the record, whereas OE captures the overall trend but exhibits more noticeable deviations in specific transient regions, in agreement with its lower Fit% in Table 2. In contrast, FIR presents the largest mismatch in key segments of the waveform, confirming that this structure is less effective for representing the $U_1 \rightarrow Y_1$ dynamics under the selected excitation and operating conditions.

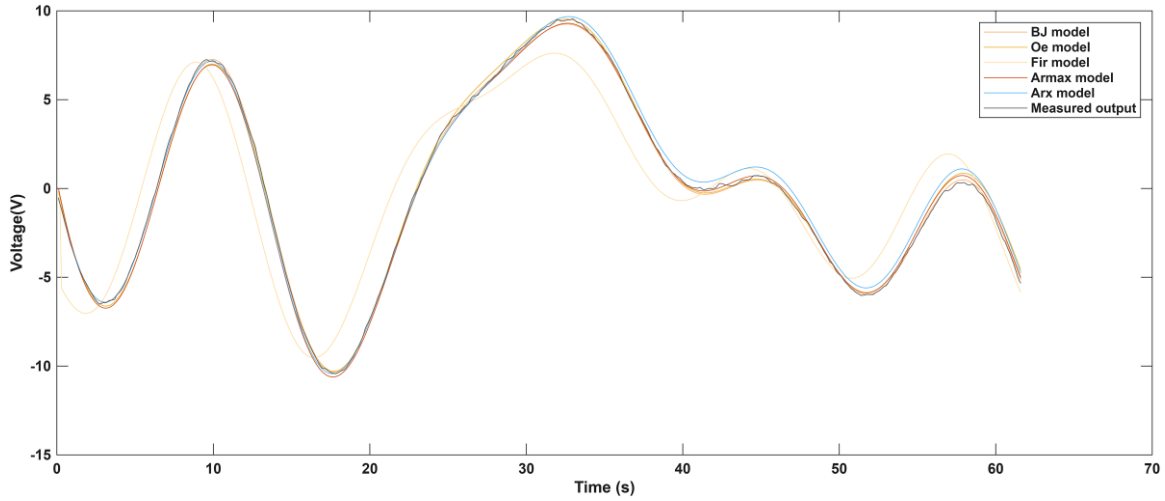

Figure 11. Comparison between measured and simulated responses for the $U_1 \rightarrow Y_1$

Figure 12 reports the residual diagnostics for the same channel. In the residual autocorrelation test (upper panel), ARX (blue), ARMAX (red), and BJ (orange) remain mostly within the confidence bounds at non-zero lags, indicating residuals closer to white. By contrast, OE (dark yellow) and FIR (yellow) exhibit clear excursions beyond the confidence bounds, indicating non-white (colored) residuals, i.e., residuals with remaining temporal correlation. In the input–residual cross-correlation test (lower panel), only the FIR model (yellow) shows a clear violation outside the confidence bounds over multiple lags, indicating that part of the residual is still explainable by the input (i.e., under-modeled deterministic input–output dynamics). Importantly, although OE (dark yellow) fails the whiteness test (autocorrelation), it does not show a strong input–residual dependence, suggesting that its main limitation in this channel is related to disturbance/noise description rather than missing deterministic dynamics. Taken together with Table 2 (Fit%, AIC/BIC, and Npar), these results support selecting ARMAX as the most defensible accuracy–parsimony choice for the $U_1 \rightarrow Y_1$ pathway, while BJ remains a high-fit alternative with higher complexity.

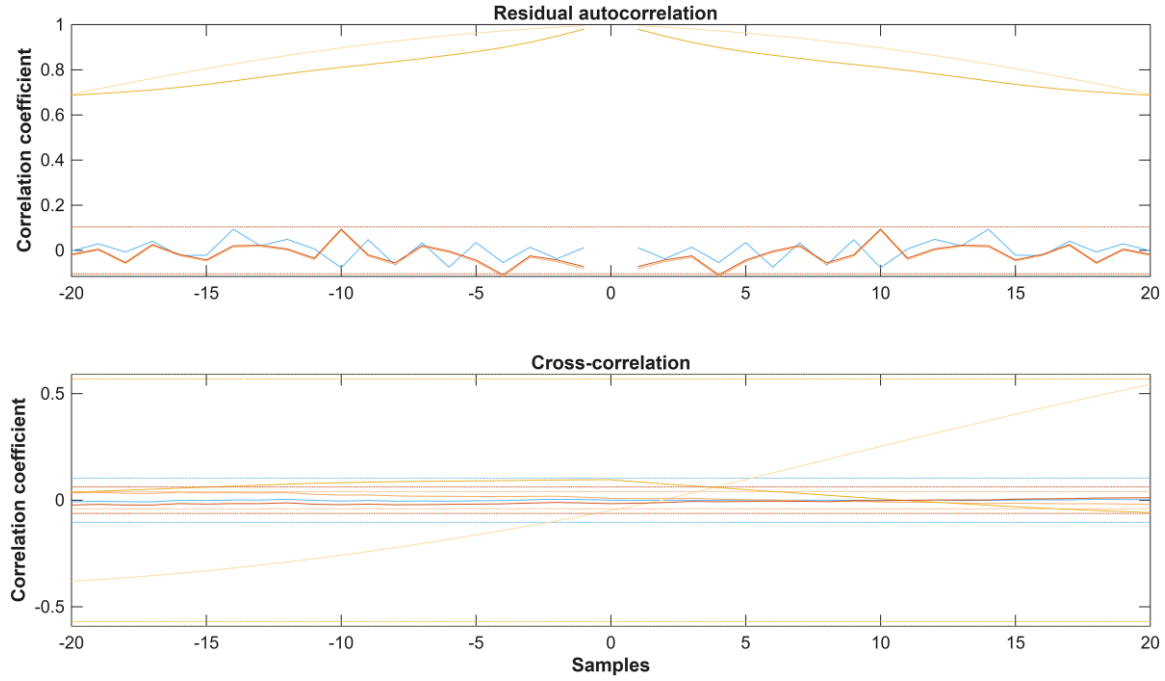

Figure 12. Residual diagnostics for MIMO parametric models $U_1 \rightarrow Y_1$

Figure 13 compares the measured output Y_2 against the simulated responses obtained with the candidate parametric structures for the $U_1 \rightarrow Y_2$ pathway. In this channel, the fit differences reported in Table 2 are reflected in the time-domain behavior: the BJ model provides the closest overall reproduction of the measured waveform across the validation horizon, capturing the dominant oscillatory content with the smallest phase and amplitude deviations among the candidates. In contrast, the remaining structures exhibit markedly poorer agreement in this pathway, with visible mismatch in amplitude and/or phase over repeated cycles, which is consistent with their substantially lower Fit% values in Table 2. These results indicate that $U_1 \rightarrow Y_2$ is a comparatively more challenging pathway to model with compact ARX/ARMAX/OE/FIR structures under the current excitation and operating conditions, and it tends to require a more flexible parametrization to reach an acceptable time-domain match.

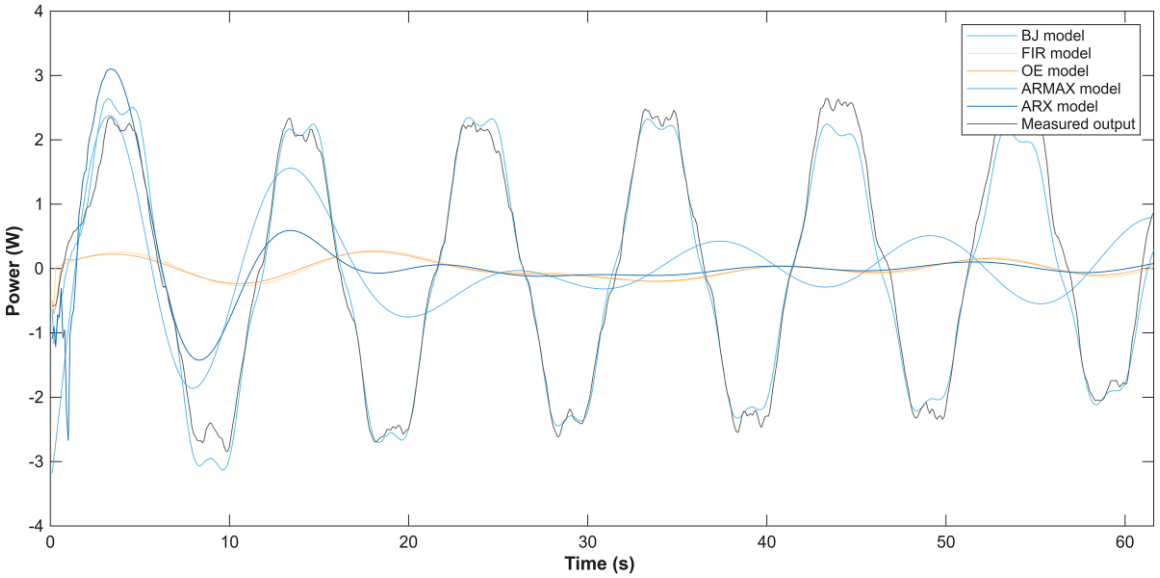

Figure 13. Comparison between measured and simulated responses for the $U_1 \rightarrow Y_2$

Figure 14 reports the residual diagnostics for the $U_1 \rightarrow Y_2$ pathway. In the residual autocorrelation test (upper panel), OE (orange) and FIR (yellow) exhibit clear excursions beyond the confidence bounds at non-zero lags, indicating non-white (colored) residuals, i.e., remaining temporal correlation in the error sequence. In contrast, BJ (light blue), ARMAX (blue), and ARX (dark blue) remain mostly within the confidence bounds over the inspected lag range, suggesting comparatively cleaner residual behavior for this channel. In the input–residual cross-correlation test (lower panel), all models remain within the confidence bounds, indicating no statistically significant dependence between the residual and the input over the evaluated lags. Therefore, the main deficiency observed for OE and FIR is primarily associated with residual coloration (stochastic consistency) rather than missing deterministic input–output dynamics. Taken together with Table 2 (Fit%, AIC/BIC, and Npar), these results support selecting BJ as the most defensible accuracy choice for the $U_1 \rightarrow Y_2$ pathway.

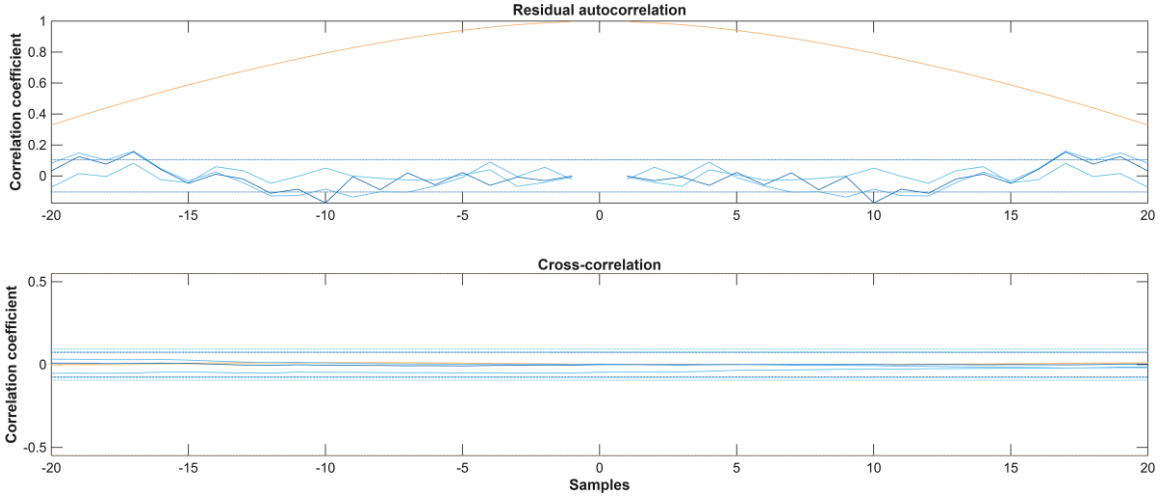

Figure 14. Residual diagnostics for MIMO parametric models $U_1 \rightarrow Y_2$

Figure 15 compares the measured output Y_1 against the simulated responses obtained with the candidate parametric structures for the $U_2 \rightarrow Y_1$ pathway. The time-domain comparison shows that ARX, ARMAX, and BJ provide an excellent reproduction of the measured waveform, with near-overlap across most of the validation horizon and only minor deviations around sharp transitions. In contrast, OE and FIR yield responses that remain at a much smaller amplitude and are visibly detached from the measured trajectory over the entire record, indicating that these structures do not capture the dominant input–output dynamics for this channel under the present identification setting. This observation is consistent with Table 2, where the top-ranked candidates (ARMAX/BJ/ARX) achieve uniformly high Fit% values (≈99.4%). Since predictive accuracy among these top candidates is essentially comparable, the final choice is primarily driven by parsimony and complexity-penalized criteria: ARMAX achieves a Fit% comparable to BJ and ARX while using fewer parameters (Npar = 8 versus 14 and 16, respectively) and maintaining competitive AIC/BIC values, making it the most defensible control-oriented option for $U_2 \rightarrow Y_1$.

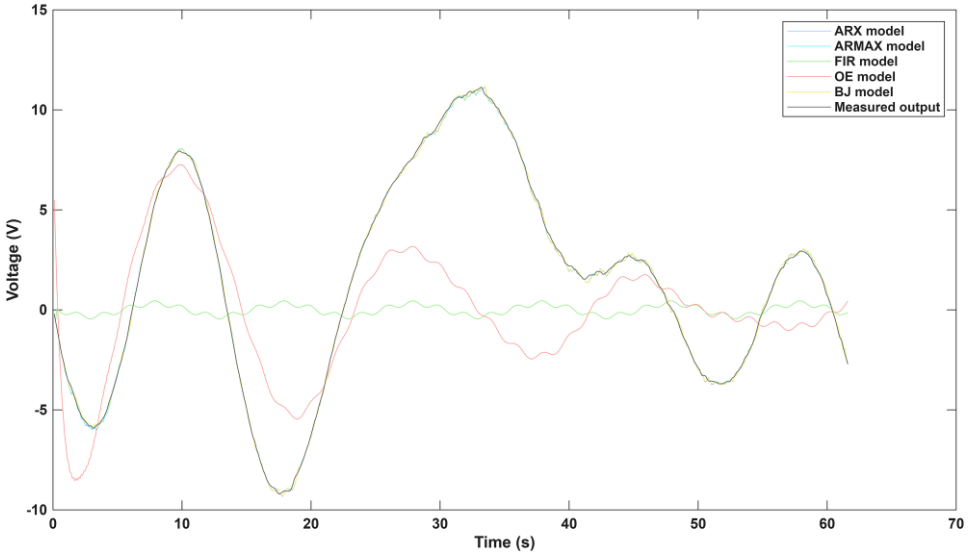

Figure 15. Comparison between measured and simulated responses for the $U_2 \rightarrow Y_1$

Figure 16 reports the residual diagnostics for the same channel. In the residual autocorrelation test (upper panel), ARX (blue), ARMAX (light blue/cyan), and BJ (yellow) remain mostly within the confidence bounds at non-zero lags, indicating residuals close to white and limited remaining temporal structure in the error. By contrast, OE (orange) and FIR (green) exhibit clear excursions beyond the confidence bounds, indicating non-white (colored) residuals. In the input–residual cross-correlation test (lower panel), only OE violates the confidence bounds, suggesting that part of its residual remains explainable by the input and therefore that some deterministic input–output dynamics are not fully captured by this structure in the present setting. Conversely, the remaining models stay within the confidence limits, indicating no statistically significant input–residual dependence over the inspected lags. Taken together with Table 2 (Fit%, AIC/BIC, and Npar), these results support selecting ARMAX as the most defensible accuracy–parsimony choice for the $U_2 \rightarrow Y_1$ pathway, while BJ remains a high-fit alternative with higher complexity.

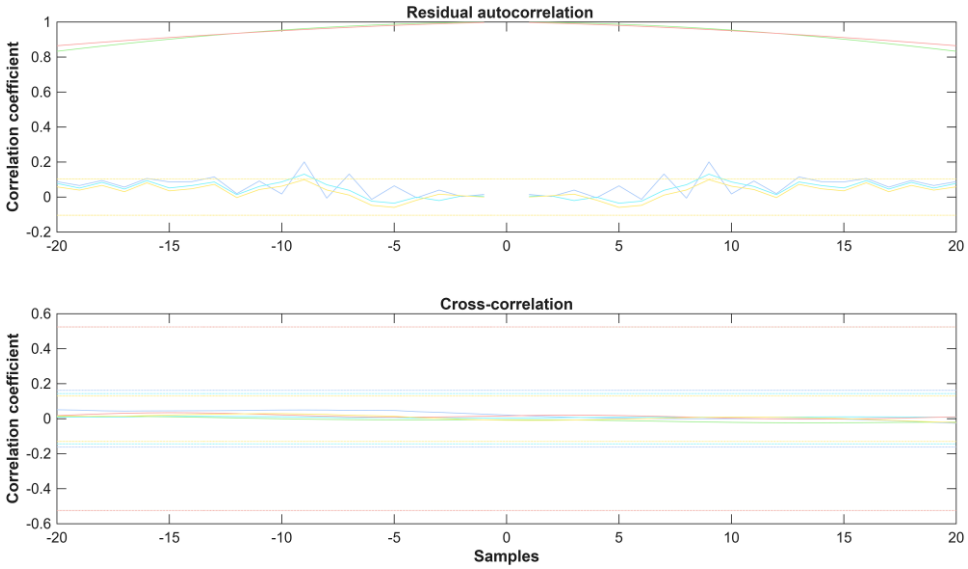

Figure 16. Residual diagnostics for MIMO parametric models $U_2 \rightarrow Y_1$

Figure 17 compares the measured output Y_2(power) against the simulated responses obtained with the candidate parametric structures for the $U_2 \rightarrow Y_2$ pathway. The time-domain comparison shows that ARX, ARMAX, and BJ track the measured waveform closely over most of the validation horizon, capturing the dominant oscillatory pattern and the main peak/trough amplitudes with only minor deviations near sharp transitions. OE reproduces the overall trend but exhibits slightly larger deviations in some segments, particularly around peak regions where the measured signal presents sharper features. In contrast, FIR shows pronounced oscillatory behavior and a visibly detached trajectory relative to the measured output, indicating that this structure does not capture the dominant dynamics of the $U_2 \rightarrow Y_2$ channel under the present identification setting. These observations are consistent with Table 2, where the top-ranked candidates for this channel exhibit very similar Fit% values (≈93%), and model preference is therefore largely driven by complexity-aware criteria and statistical validation rather than by time-domain accuracy alone.

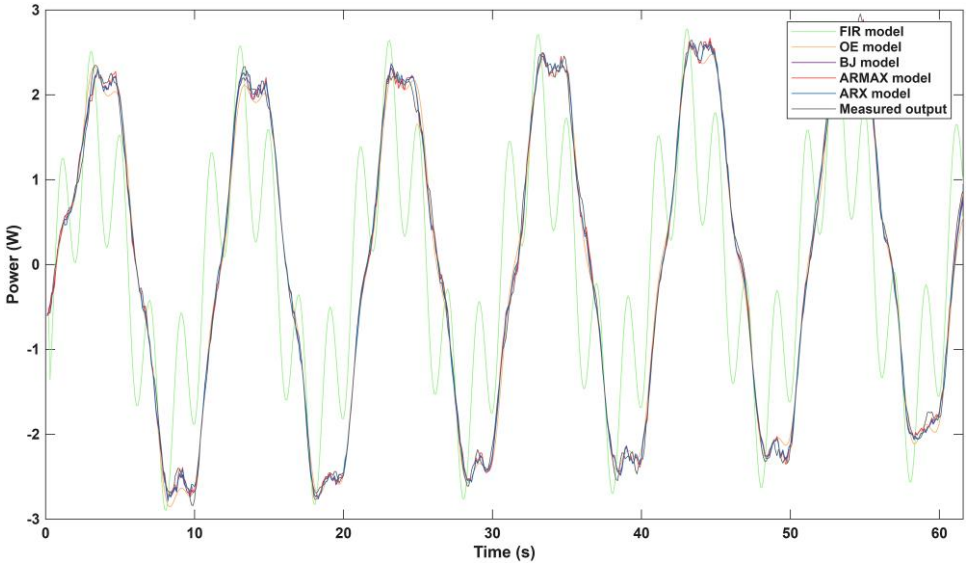

Figure 17. Comparison between measured and simulated responses for the $U_2 \rightarrow Y_2$

Figure 18 reports the residual diagnostics for the same channel. In the residual autocorrelation test (upper panel), ARX (blue), ARMAX (red), and BJ (purple) remain mostly within the confidence bounds at non-zero lags, indicating residuals closer to white and limited remaining temporal structure in the error. By contrast, OE (orange) and FIR (green) exhibit clear excursions beyond the confidence bounds, indicating non-white (colored) residuals. In the input–residual cross-correlation test (lower panel), only FIR (green) violates the confidence bounds, indicating that part of its residual remains explainable by the input and therefore that deterministic input–output dynamics are still under-modeled by this structure. Taken together with Table 2 (Fit%, AIC/BIC, and Npar), these results support selecting ARMAX as a compact and statistically consistent accuracy–parsimony choice for the $U_2 \rightarrow Y_2$ pathway, while BJ remains a competitive high-fit alternative supported by favorable information criteria at a slightly higher parameter count.

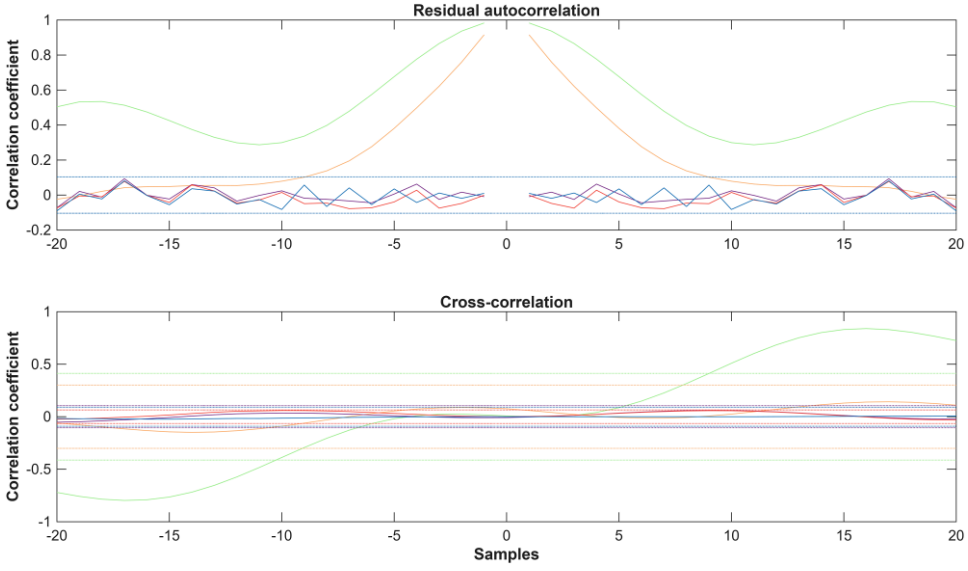

Figure 18. Residual diagnostics for MIMO parametric models $U_2 \rightarrow Y_2$

5-4- Results of the Grey-Box PEMFC Model

After tuning the grey-box model parameters as described in Subsection 4.5, its performance was evaluated using an independent validation dataset. Figure 19 compares the measured and simulated responses for the two outputs: cell voltage Y_1(top) and stack power Y_2(bottom). The grey-box model shows excellent agreement with the validation data, achieving 97.35% Fit for Y_1 and 86.47% Fit for Y_2. The voltage dynamics are captured with high accuracy, whereas the power response is reproduced with adequate fidelity given its stronger nonlinear dependence on both voltage and load current. The remaining mismatch in Y_2 is mainly observed near steep transitions, where the nonlinear coupling is strongest. Overall, these results confirm that the grey-box model provides a compact yet physically interpretable representation of PEMFC dynamics and can serve as a solid basis for control-oriented modeling and simulation studies [10, 18].

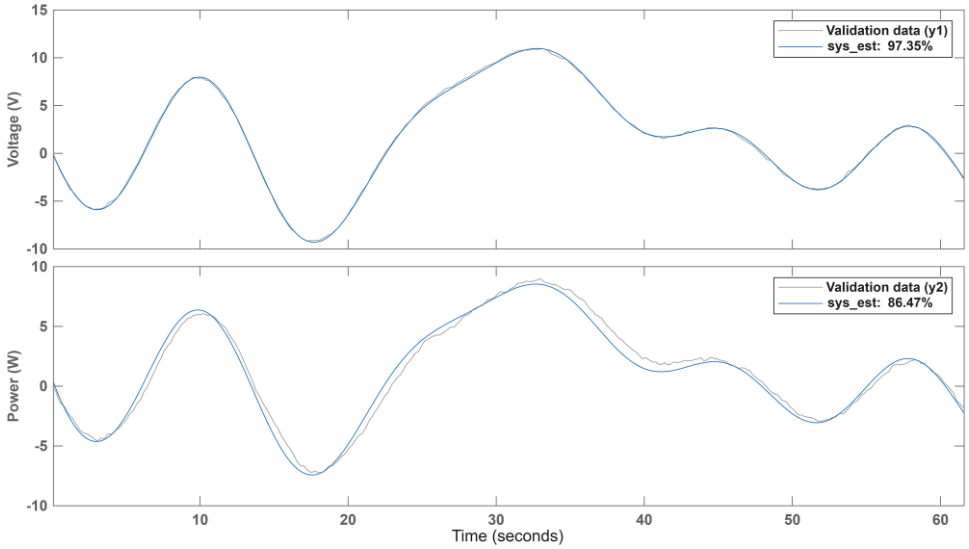

Figure 19. Comparison between validation data and grey-box model responses for voltage Y_1(top) and power Y_2(bottom)

5-5- Discussion and Practical Implications

This section interprets the identification results from a control-oriented perspective. First, the operating conditions used to define the small-signal regime are stated explicitly, and the expected loss of validity as the operating point shifts is discussed. Second, the implications of PEMFC nonlinearities, particularly water management and membrane hydration, on the CRA-based non-parametric baseline and on the residual behavior of parametric models are examined. Third, the results obtained are contextualized by comparison against previous PEMFC identification research. Finally, the accuracy–parsimony rationale behind the selected model structures in SISO and MIMO is summarized, using Fit% together with complexity-penalized criteria (AIC/BIC) and residual diagnostics to justify which candidates are most suitable for control and energy-management applications.

An additional SISO identification experiment was conducted at a shifted operating condition to assess the sensitivity of the identified dynamics to changes in the operating regime. The operating point was set to $i_0 = 0.00575\ \mathrm{A/cm^2}$ ($+15\%$ relative to $0.005\ \mathrm{A/cm^2}$), $T = 358\ \mathrm{K}$, and $P_{H_2} = P_{O_2} = 1.20\ \mathrm{atm}$ ($P_{\mathrm{ref}} = 1\ \mathrm{atm}$). Under these conditions, the stack Nernst voltage increases to $E_{\mathrm{Nernst}} \approx 12.07\ \mathrm{V}$. Figure 20 reports the 5-step prediction performance on independent validation data. The shifted-point identification preserves high predictive accuracy and a consistent ranking across candidate structures: BJ achieves the best fit (87.28%), followed closely by ARMAX (86.66%) and ARX (86.62%). In contrast, OE provides a lower fit (80.87%), while the simplified low-memory baseline (FIR-equivalent) yields the lowest performance (67.88%). Overall, these results suggest that moderate changes in (i_0, T, P)under bounded excitation do not fundamentally alter the dominant SISO dynamics captured by the proposed control-oriented identification workflow, whereas more constrained structures (OE/FIR) become less competitive.

CRA provides a convenient non-parametric baseline, but it relies on quasi-linear and time-invariant behavior over the analyzed window. Consequently, nonlinearities driven by water management and membrane hydration may affect CRA by introducing slow drift or regime changes that effectively smear the estimated impulse/FRF and increase residual correlation. Under small-signal operation, reported water-management effects suggest that hydration/flooding states can induce millivolt-level voltage variations at the single-cell level; for instance, a fuzzy model validated via spectroscopy

reported voltage changes on the order of 1–5.2 mV between dry and flooded conditions [25]. For a 12 V-class stack (≈17 cells at ~0.7 V/cell), this corresponds to an aggregated variation on the order of tens of millivolts, which is typically small relative to the nominal stack voltage and therefore compatible with control-oriented linearization assumptions in many applications [26]. Accordingly, under bounded multisine excitation and fixed operating conditions, CRA remains a reliable first-step baseline in the present workflow. However, if hydration dynamics become dominant (*e.g.*, longer windows, larger excursions, or rapid RH variations), CRA estimates are expected to show reduced consistency and stronger residual structure. In such cases, segment-wise CRA, time-varying identification, or nonlinear frequency-response tools based on higher-order harmonic information become more appropriate for capturing nonlinear distortions beyond the first-order response [27].

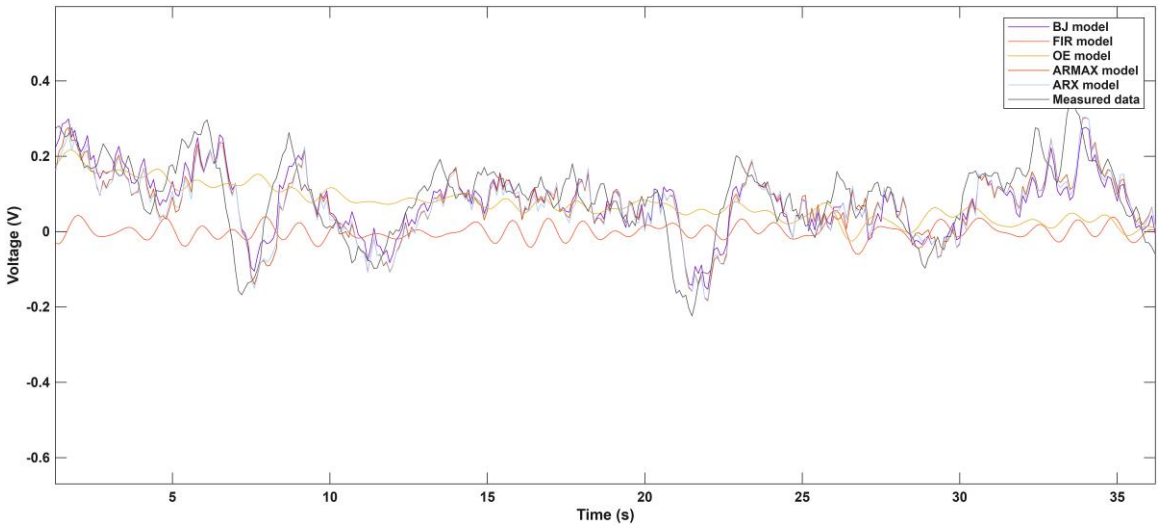

Figure 20. SISO identification at a shifted operating point

The observed accuracy–parsimony trade-off is consistent with recent identification-oriented PEMFC literature. Black-box system identification has been shown to yield compact PEMFC models suitable for prediction and control, while emphasizing the need to balance predictive accuracy against model complexity [28]. More recent work has highlighted that operating conditions and time-varying effects can challenge fixed-parameter linear models under frequent load changes. For instance, online adaptive modeling has been proposed to cope with nonlinear/time-varying voltage dynamics by updating parameters during operation [29]. Furthermore, PEMFC system-identification studies reporting validation across operating conditions reinforce the importance of combining time-domain accuracy with model-consistency checks when selecting structures for control-oriented use [30]. The contribution of the proposed identification system achieves high fit, as well as, an unified and reproducible workflow that links: (i) multisine/CRA non-parametric baselines, (ii) low-order parametric structures screened with information criteria and residual diagnostics, and (iii) a compact grey-box state-space model validated on independent data, thereby offering practical guidance on structure choice under accuracy–parsimony and statistical-consistency requirements.

Across the full set of SISO and MIMO experiments, the results confirm that model preference must be decided by a joint criterion of time-domain Fit%, complexity penalties (AIC/BIC) and Npar, and residual consistency, rather than Fit% alone. In SISO, Box–Jenkins achieves a Fit of 98.75%, while ARMAX offers the most defensible control-oriented compromise (Fit = 96.84%) because it achieves the lowest AIC/BIC with residual behavior mostly within confidence bounds. In MIMO, channel-wise outcomes reveal two regimes. For the dominant voltage pathways, compact structures are sufficient: $U_1 \rightarrow Y_1$ is well captured by ARMAX (Fit = 97.85%, Npar = 6), with BJ close behind (97.23%, Npar = 8), and $U_2 \rightarrow Y_1$ reaches ≈ 99.4% Fit for BJ/ARX/ARMAX, where parsimonia and residual tests favor ARMAX (Npar = 8) over higher-parameter alternatives. The most challenging coupled pathway is $U_1 \rightarrow Y_2$, where only a richer stochastic description attains acceptable accuracy (BJ: 86.38%, Npar = 15), while lower-order ARX/ARMAX provide poor fits under the same setting. For $U_2 \rightarrow Y_2$, fits are close (≈93%), and information criteria together with residual diagnostics guide the final preference against models leaving input-correlated residuals. Residual autocorrelation and input–residual cross-correlation tests systematically distinguish residual coloration (imperfect disturbance/noise description) from missing deterministic dynamics, supporting the final channel-wise selections. Finally, the grey-box state-space model complements the black-box results by providing a compact, physically interpretable representation with strong validation performance of 97.35% fit for voltage and 86.47% fit for power, serving as a transparent baseline for simulation and control-oriented studies.

6- Conclusion

Accurate and compact dynamic models of PEM fuel cells are essential for control and energy-management design; however, identification is challenging due to nonlinear coupling and constrained excitation. This paper presented a sequential hybrid identification workflow to obtain control-oriented discrete-time SISO and MIMO models of a PEMFC plant using a nonlinear MATLAB/Simulink controlled simulation environment. The plant was fixed at a selected operating point and excited with bounded multisine inputs designed to ensure persistent excitation over a prescribed frequency band while respecting physically admissible constraints. Input–output data were pre-processed and first analyzed using CRA to establish a non-parametric baseline (FRF/impulse dynamics), which then informed subsequent parametric identification (ARX, ARMAX, OE, BJ, FIR) and grey-box state-space modeling.

A central contribution is the transparent model-selection strategy combining validation Fit% with complexity-penalized criteria (AIC/BIC), parameter count (Npar), and residual diagnostics (residual autocorrelation and input–residual cross-correlation), enabling defensible structure choice beyond Fit% alone. In the SISO case, BJ achieved the highest agreement with validation data (Fit = 98.75%), whereas ARMAX provided the most robust accuracy–parsimony compromise (Fit = 96.84% with the lowest AIC/BIC and residual behavior mostly within confidence bounds). In the MIMO configuration, channel-wise identification showed high accuracy in the dominant pathways (e.g., $U_1 \rightarrow Y_1$: 97.85% and $U_2 \rightarrow Y_1$: ≈99.4%), while the most coupled pathway remained the limiting case ($U_1 \rightarrow Y_2$: best Fit = 86.38% with BJ), indicating when richer stochastic structures are necessary. The grey-box model complemented the black-box candidates by providing a compact, physically interpretable representation with strong validation performance (97.35% fit for voltage and 86.47% for power). All results are based on repeatable simulation data, enabling controlled excitation and fair benchmarking across model classes.

Future work will extend the workflow beyond a single operating point via multi-model/LPV scheduling, incorporate humidity and water-management dynamics, and validate the approach on experimental stack data under actuator constraints, measurement bias, and aging effects.

7- Declarations

7-1- Author Contributions

Conceptualization, E.B.-F.; methodology, E.B.-F.; software, E.B.-F.; validation, E.B.-F.; formal analysis, E.B.-F., A.R.-R., W.A., and E.V.-A.; investigation, E.B.-F.; resources, E.B.-F., A.R.-R., W.A., and E.V.-A.; data curation, E.B.-F.; writing—original draft preparation, E.B.-F.; writing—review and editing, A.R.-R., W.A. and E.V.-A.; visualization, E.B.-F.; supervision, A.R.-R.; project administration, A.R.-R. All authors have read and agreed to the published version of the manuscript.

7-2- Data Availability Statement

The data presented in this study are available on request from the corresponding author. The data are not publicly available because they consist of MATLAB/Simulink-generated simulation outputs and model files that require curated packaging for reuse.

7-3- Funding

The authors received no financial support for the research, authorship, and/or publication of this article.

7-4- Acknowledgments

The authors would like to acknowledge the support of Escuela Superior Politécnica del Litoral (ESPOL) for the technical and academic resources provided during this research. They are also grateful to their colleagues and advisors for their guidance and contributions to the model development and validation.

7-5- Institutional Review Board Statement

Not applicable.

7-6- Informed Consent Statement

Not applicable.

7-7- Conflicts of Interest

The authors declare that there is no conflict of interest regarding the publication of this manuscript. In addition, the ethical issues, including plagiarism, informed consent, misconduct, data fabrication and/or falsification, double publication and/or submission, and redundancies have been completely observed by the authors.

8- References

[1] Benavides-Farias, E., Rubio-Roldan, A., Agila, W., & Munoz-Zurita, L. (2024). Implementation of Proton Exchange Membrane Fuel Cells in Agricultural Areas: Technical and Economic Benefits. 13th International Conference on Renewable Energy Research and Applications, ICRERA 2024, 617–622. doi:10.1109/ICRERA62673.2024.10815342.

[2] Rubio-Roldán, A., Aviles, J. C., & Bustos-Painni, E. (2025). Comparison of Alternatives for Rural Electrification in Ecuador: Case Study of Islets in the Gulf of Guayaquil. Conference Proceedings - 2025 IEEE International Conference on Environment and Electrical Engineering and 2025 IEEE Industrial and Commercial Power Systems Europe, EEEIC / I and CPS Europe 2025. doi:10.1109/EEEIC/ICPSEurope64998.2025.11169255.

[3] Rubio, A., Agila, W., González, L., & Aviles-Cedeno, J. (2023). Distributed Intelligence in Autonomous PEM Fuel Cell Control. Energies, 16(12), 4830. doi:10.3390/en16124830.

[4] Barbir, F. (2012). PEM fuel cells: Theory and practice. PEM Fuel Cells: Theory and Practice. Academic Press, Amsterdam, Netherland. doi:10.1016/C2011-0-06706-6.

[5] Ansari, A. B. (2023). Reduced-order modeling of PEM fuel cell based on POD and PODI: an efficient approach toward combining highest accuracy with real-time performance. International Journal of Hydrogen Energy, 48(75), 29327–29349. doi:10.1016/j.ijhydene.2023.04.096.

[6] Zhang, Z., Cai, S. J., Cheng, J. H., Guo, H. B., & Tao, W. Q. (2025). A comprehensive system simulation from PEMFC stack to fuel cell vehicle. Applied Energy, 401, 126678. doi:10.1016/j.apenergy.2025.126678.

[7] Rojas, A. C., Lopez, G. L., Gomez-Aguilar, J. F., Alvarado, V. M., & Torres, C. L. S. (2017). Control of the air supply subsystem in a PEMFC with balance of plant simulation. Sustainability (Switzerland), 9(1), 73. doi:10.3390/su9010073.

[8] Ariza, H. E., Correcher, A., Sánchez, C., Pérez-Navarro, Á., & García, E. (2018). Thermal and electrical parameter identification of a proton exchange membrane fuel cell using genetic algorithm. Energies, 11(8), 2099. doi:10.3390/en11082099.

[9] Hjalmarsson, H. (2009). System identification of complex and structured systems. European Journal of Control, 15(3–4), 275–310. doi:10.3166/EJC.15.275-310.

[10] Jenei, S., Szalai, S. M., Singh, D. P., Afadzinu, K. S., Poyda-Nosyk, N., Kálmán, B. G., & Dávid, L. D. (2025). Europe's Energy Shift: From Fossil Fuels to Renewable Energy. Emerging Science Journal, 9(5), 2384–2399. doi:10.28991/ESJ-2025-09-05-06.

[11] Naidu, I. E. S., Padmavathi, T., Padmavathi, S. V., & Kumar, B. U. (2025). Intelligence Based Controlling Models for Effective Power Tracking and Voltage Enhancement in Grid-PV Systems. Emerging Science Journal, 9(1), 261–283. doi:10.28991/ESJ-2025-09-01-015.

[12] Vighio, A. A., Zakaria, R., Ahmad, F., & Aminuddin, E. (2025). Real-Time Monitoring and Development of a Localized OTTV Equation for Building Energy Performance. Civil Engineering Journal, 11(2), 544–564. doi:10.28991/CEJ-2025-011-02-09.

[13] Yauri, R., Cuyubamba, L., & Nuñez, S. (2025). Crop Monitoring System Using IoT, Solar Energy and Decision Tree Algorithm. Emerging Science Journal, 9(2), 603–614. doi:10.28991/ESJ-2025-09-02-06.

[14] Oyewola, O. M., Idowu, E. T., Labiran, M. J., Hatfield, M. C., & Drabo, M. L. (2026). Performance Evaluation of Inclined-Step and Wall Roughness on Battery Thermal Management System. Emerging Science Journal, 10(1), 1–19. doi:10.28991/ESJ-2026-010-01-01.

[15] Zhang, G., Qu, Z., Tao, W. Q., Mu, Y., Jiao, K., Xu, H., & Wang, Y. (2024). Advancing next-generation proton-exchange membrane fuel cell development in multi-physics transfer. Joule, 8(1), 45-63. doi:10.1016/j.joule.2023.11.015.

[16] Elkholy, M., Boureima, A., Kim, J., & Aziz, M. (2025). Data-driven modeling and prediction of PEM fuel cell voltage response to load transients for energy applications. Energy, 335, 138047. doi:10.1016/j.energy.2025.138047.

[17] Ljung, L. (1999). System identification: Theory for the user (2nd ed.). Prentice Hall, New Jersey, United States.

[18] Tangirala, A. K. (2014). Principles of System Identification: Theory and Practice. Principles of System Identification: Theory and Practice. CRC Press, Florida, United States. doi:10.1201/9781315222509.

[19] Chatfield, C., Bendat, J. S., & Piersol, A. G. (1987). Random Data: Analysis and Measurement Procedures. In Journal of the Royal Statistical Society. Series A (General), 150(2), 2981634. Wiley. doi:10.2307/2981634.

[20] Pintelon, R., & Schoukens, J. (2012). System Identification: A Frequency Domain Approach. Encyclopedia of Systems and Control (2nd ed.). Wiley-IEEE Press, New Jersey, United States.

[21] MathWorks. (2024). System Identification Toolbox User's Guide. The MathWorks, Inc., Natick, United States. Available online: https://www.mathworks.com/help/ident/ (accessed on May 2026).

[22] Kallel, A. Y., & Kanoun, O. (2022). Crest Factor Optimization for Multisine Excitation Signals with Logarithmic Frequency Distribution Based on a Hybrid Stochastic-Deterministic Optimization Algorithm. Batteries, 8(10), 176. doi:10.3390/batteries8100176.

[23] Konishi, S., & Kitagawa, G. (2008). Information Criteria and Statistical Modeling. Springer, New York, United States. doi:10.1007/978-0-387-71887-3.

[24] Phillips, C. R., & Nagle, N. T. (2012). Digital control system analysis and design. In IEEE Transactions on Systems, Man, and Cybernetics: Vol. SMC-15. Pearson Education, New Jersey, United States.. doi:10.1109/tsmc.1985.6313385.

[25] Rubio, G. A., & Agila, W. E. (2021). A fuzzy model to manage water in polymer electrolyte membrane fuel cells. Processes, 9(6), 904. doi:10.3390/pr9060904.

[26] Rubio Roldán, A. (2021). Un novel modelo dinámico de la pila de combustible tipo PEM en un contexto estratégico (Tesis doctoral, Universidad Nacional de Cuyo). Repositorio Digital UNCuyo. Available online: https://bdigital.uncu.edu.ar/20187 (accessed on May 2026).

[27] Yuan, H., Zhou, S., Zhang, S., Tang, W., Jiang, B., Wei, X., & Dai, H. (2024). Unconventional frequency response analysis of PEM fuel cell based on high-order frequency response function and total harmonic distortion. Applied Energy, 357, 122489. doi:10.1016/j.apenergy.2023.122489.

[28] Chavan, S. L., & Talange, D. B. (2018). System identification black box approach for modeling performance of PEM fuel cell. Journal of Energy Storage, 18, 327–332. doi:10.1016/j.est.2018.05.014.

[29] Zou, W., Froning, D., Shi, Y., & Lehnert, W. (2021). An online adaptive model for the nonlinear dynamics of fuel cell voltage. Applied Energy, 288, 116561. doi:10.1016/j.apenergy.2021.116561.

[30] Pinagapani, A. K., Mani, G., Chandran, K. R., Pandian, K., Sawantmorye, E., & Vaghela, P. (2021). Dynamic Modeling and Validation of PEM Fuel Cell via System Identification Approach. Journal of Electrical Engineering and Technology, 16(4), 2211–2220. doi:10.1007/s42835-021-00736-2.